Astronomy & Astrophysics manuscript no. XSGRB_sample
Tuesday 3rd January, 2017

A&A proofs: manuscript no. XSGRB_sample

©ESO 2017

XSGRB - The X-shooter GRB afterglow sample

J. Selsing[1], D. Malesani[1], T. Krühler[1], J. P. U. Fynbo[1], P. Goldoni[14], A. de Ugarte Postigo[11], J. Japelj[20], P. D'Avanzo, Z. Cano, S. Covino[10], V. D'Elia[7,12], H. Flores, O. E. Hartoog[6], J. Hjorth[1], P. Jakobsson[5], A. Levan, A. Melandri, S. Piranomonte[7], R. Sánchez-Ramírez[11], S. Schulze[17,18], N. R. Tanvir[19], C. Thöne, S. D. Vergani[7,8], P. M. Vreeswijk[3], D. J. Watson[1], K. Wiersema[19], D. Xu[1] L. Christensen[1], A. De Cia[3], L. Kaper[6], L. A. Antonelli, F. Fiore, A. Gomboc, P. Groot, F. Hammer, C. Ledoux[2], E. Maiorano, B. Milvang-Jensen[1], E. Palazzi, E. Pian, J. Schaye, G. Tagliaferri[7], R. A. M. J. Wijers[6]

1   Dark Cosmology Centre, Niels Bohr Institute, University of Copenhagen, Juliane Maries Vej 30, 2100 København Ø, Denmark
2   European Southern Observatory, Alonso de Córdova 3107, Vitacura, Casilla 19001, Santiago 19, Chile
3   Department of Particle Physics and Astrophysics, Faculty of Physics, Weizmann Institute of Science, Rehovot 76100, Israel
4   Thüringer Landessternwarte Tautenburg, Sternwarte 5, 07778 Tautenburg, Germany
5   Centre for Astrophysics and Cosmology, Science Institute, University of Iceland, Dunhagi 5, IS-107 Reykjavik, Iceland
6   Astronomical Institute Anton Pannekoek, University of Amsterdam, Science Park 904, NL-1098 XH Amsterdam, the Netherlands
7   INAF-Osservatorio Astronomico di Roma, Via Frascati 33, I-00040 Monteporzio Catone, Italy
8   GEPI-Observatoire de Paris, CNRS UMR 8111, Univ. Paris-Diderot, 5 Place Jules Janssen - 92190 Meudon, France
9   American River College, Physics and Astronomy Dpt., 4700 College Oak Drive, Sacramento, CA 95841, USA
10 INAF, Osservatorio Astronomico di Brera, Via E. Bianchi 46, I-23807 Merate, Italy
11 Instituto de Astrofísica de Andalucía (IAA-CSIC), Glorieta de la Astronomía s/n, 18008, Granada, Spain
12 ASI-Science Data Centre, Via Galileo Galilei, I-00044 Frascati, Italy
13 Institute of Experimental and Applied Physics, Czech Technical University in Prague, Horska 3a/22, 128 00 Prague 2, Czech Republic
14 APC, Astroparticules et Cosmologie, Universite Paris Diderot, CNRS/ IN2P3, CEA/Irfu, Observatoire de Paris, Sorbonne Paris Cite, 10, Rue Alice Domon et L eonie Duquet, 75205 Paris Cedex 13, France
15 Max-Planck-Institut für extraterrestrische Physik, Giessenbachs traße, 85748 Garching, Germany
16 Università degli studi di Milano-Bicocca, Piazza della Scienza 3, 20126, Milano, Italy
17 Pontificia Universidad Católica de Chile, Departamento de Astro nomía y Astrofísica, Casilla 306, Santiago 22, Chile
18 Millennium Center for Supernova Science
19 Department of Physics and Astronomy, University ofLeicester, University Road, Leicester, LE1 7RH, UK
20 University of Ljubljana,Department of Physics,Faculty of Mathematics & Physics,SI

ABSTRACT

The *Swift* satellite allows us to use gamma-ray bursts (GRBs) to peer into the hearts of star forming galaxies through cosmic time. Our open collaboration, representing most of the active ESO member researchers in this field, seeks to build a public legacy sample of GRB X-shooter spectroscopy while *Swift* continues to fly. We propose to continue our programme to target all suitably observable GRB afterglows (up to 15 bursts per semester), with the primary goal of producing a well-defined, homogeneous, statistically useful sample. To date, our spectroscopy covers a redshift range from 0.059 to about 8, with more than 20 robust metallicity measurements from absorption lines (over the redshift range 1.7–5.9) and 4 secure detections of H_2 or CH molecular absorption. Such information is extremely difficult to obtain by other means. In terms of studying the spread and redshift evolution in gas-phase properties, the sample is still limited by low-number statistics.

Key words. Gamma-ray burst: individual: GRB 120815A — galaxies: high-redshift — ISM: molecules — dust, extinction

1. Introduction

Only after observing more than 12000 damped Lyman-α absorbers (DLAs) towards about 10^5 QSOs have 5 systems with $\log(N_{HI}/cm^{-2}) > 22$ been identified (Noterdaeme et al. 2012). Long GRB afterglow spectra, by contrast, reveal such systems in the majority of cases (Jakobsson et al. 2006; Fynbo et al. 2009). Whereas DLAs towards QSOs are mostly limited to $1.8 \lesssim z \lesssim 5$ due to the atmospheric UV-cutoff and increasing Lyman-blanketing at increasing redshifts (e.g., Rafelski et al. 2014), GRBs allow us to see into the hearts of star-forming galaxies over the full history of cosmic star formation from $z \approx 0$ to $z > 8$ (e.g., Tanvir et al. 2009; Salvaterra et al. 2009; Jakobsson et al. 2012). With afterglow spectroscopy (throughout the electromagnetic spectrum from X-rays to the sub-mm) we can hence characterize the properties of star-forming galaxies over cosmic history in terms of redshifts, metallicities, molecular contents, ISM temperatures, UV-flux densities, etc.. This is, however, only possible as long as there are satellites in orbit that rapidly and

---

accurately locate GRBs. The currently operating *Swift* satellite, launched in 2004 and still fully-functioning, allows for very efficient follow-up observations of GRBs due to its unprecedented rate, speed and precision of localisations.

There are several unanswered but fundamental questions that must be addressed in order to exploit the full potential of GRBs as cosmological probes. More than 50% of the *Swift* bursts with measured redshift are at $z > 2$, and 5–10% are expected to be above $z = 5$ (Salvaterra et al. 2007, 2012; Jakobsson et al. 2012; Perley et al. 2016). A high redshift completeness is crucial for our understanding of the link between the number density of GRBs per unit redshift and the global star-formation history of the Universe, as measured by other means (UV, FIR, sub-mm, see Robertson & Ellis 2012). The detection of GRBs at $z > 6$ shows that GRBs have become competitive as a tool to identifying galaxies at the highest redshifts and unsurpassed in providing detailed abundance information via absorption line spectroscopy (Tanvir et al. 2012; McGuire et al. 2016).

From March 2005 to March 2016 there have been about 350 *Swift* bursts complying with our sample selection criteria (see "Immediate objective"), and about half of them have measured redshifts. Among the latter subset, the team proposing these observations has measured about two thirds of the redshifts, mainly with FORS1/2 and X-shooter (see Fynbo et al. 2009, ApJS, 185, 526; Jakobsson et al. 2012, ApJ, 752, 62; Krühler et al. 2012, ApJ, 758, 46). Our current aim is to build a sample superior to our previous low-resolution survey (Fynbo et al. 2009, ApJS, 185, 526), both in terms of quantity and quality of the spectra. Our program started as guaranteed time observations during periods 84-91, and we have continued in open time since then.

X-shooter is in many ways the ideal GRB follow-up instrument and indeed GRB follow-up was one of the primary science cases behind the instrument design and implementation. Our program secures general purpose GRB afterglow spectroscopic follow-up that adds strong legacy value to the *Swift* GRB sample. Due to the wide wavelength range of X-shooter with the same observation cover molecular H_2 absorption near the atmospheric cut-off and all the strong emission lines from the host in the NIR arm (e.g., Friis et al., 2015, MNRAS, 451, 167). In general, the wide wavelength coverage ensures that we always have features on which to base a redshift measurement as long as the afterglow is brighter than about 23 mag in either the R- or z-band. Frequently, emission lines are also detected from the underlying host, which also provide further information such as SFR and metallicity (the top right panel in Fig. 1 shows an example). Only for 7 out of more than 70 secured spectra could we not measure a redshift. With the X-shooter survey we provide **metallicity measurements** for about 30% (Voigt-profile fits) of the $z > 1.7$ events. So far we have measured metallicities for more than 20 GRB afterglows with X-shooter. With the wide wavelength coverage of X-shooter we can study important chemical species as Zn II, Cr II and α elements over a much wider redshift range than what is possible with other instruments. As an example, we have measured a metallicity of $0.1Z_\odot$ for GRB 100219A at $z = 4.669$ (Thöne et al. 2013, MNRAS, 428, 3590), $0.02Z_\odot$ for GRB 111008A at $z = 4.991$ (Sparre et al. 2014, ApJ, 785, 150) and $0.05Z_\odot$ for the $z = 5.9125$ GRB 130606A (Hartoog et al. 2015, A&A, 580, 139). Reconciling the abundance patterns of GRB absorbers, other types of absorbers, QSO DLAs in particular, and old stars in the Local Group is an important long-term goal (see also Sparre et al. 2014, ApJ, 785, 150). Metallicities are also measured from host emission lines (Krühler et al. 2015, A&A, 581, A125). GRB spectroscopy also allows us to

determine the dust content of their environments, both through analysis of the depletion pattern and through measurement of the associated extinction (Japelj et al. 2015, A&A, 451, 2050). This allows us to quantify the dust-to-metals ratio and its evolution with redshift (e.g., De Cia et al. 2013, A&A, 560, 88; Zafar & Watson 2013, A&A, 560, 26).

We will also determine the frequency and properties of **molecular absorption** towards GRB absorbers. Molecular gas is a key element to catalyze the process of star formation, but prior to our program H_2 had been detected just in two cases (tentatively in Fynbo et al. 2006, A&A, 451, L47; securely in Prochaska et al. 2009, ApJ, 691, L27). With our X-shooter program we have found three more systems (Krühler et al. 2013, A&A, 557, 18; D'Elia et al. 2014, A&A, 564, 38; Friis et al. 2015, MNRAS, 451, 167). We are currently analysing more of our spectra for less obvious molecular absorption and we expect to find more (a dedicated sample paper is addressing this issue).

A natural question to ask is: **how long should this work continue?** Our view is that we need to keep observing the afterglows as long as we have *Swift* in operation. Also note that the program is still producing many papers and provides data for many theses (Box 9 and 10). *Swift* is currently funded until 2018, but is likely to get more extensions given its overwhelming success. As mentioned above GRBs allow us to probe star-forming galaxies that are almost impossible to study in other ways both in terms of redshifts, galaxy luminosity function, and regions within galaxies. After 7 periods we have secured seven spectra of $z > 4$ GRBs, of which three were of sufficient quality to allow abundance measurements (Thöne et al. 2013, Sparre et al. 2014, Hartoog et al. 2015). GRBs offer the only way to derive chemical abundances for the gas phase of central, actively star-forming regions of high-z galaxies. The program also maintains a very high discovery potential where we occasionally find something completely unexpected that provides interesting clues to puzzles in other fields, e.g. extinction of type Ia supernovae (Fynbo et al. 2014, A&A, 572, 12). Each of these spectra are like precious jewels – it is a type of observation that can never be repeated and a class of sightlines that can only be studied while we have operating GRB satellites.

It is also worth adding that we have build up a rather unique team spread over Europe from Granada to Reykjavik, which by now has reached a point where the distribution of night shifts, the scientific exploitation of the data is efficient and where we are open to all new members who wish to participate. As mentioned all data are public immediately.

For all of these reasons, we need to keep building up the sample of GRB afterglow spectra now as we may have to wait many years before a mission like *Swift* becomes available again.

A significant proportion of GRBs lack a bright optical afterglow ("**dark bursts**", e.g., Jakobsson et al. 2004, ApJ, 617, L21; Melandri et al. 2012, MNRAS, 421, 1265). Some of these are at the highest redshifts ($z > 6$) and their observer-frame optical emission is absorbed by the IGM. The majority, however, suffer from large dust obscuration (e.g., Perley et al. 2009, AJ, 138, 1690; Greiner et al. 2011, A&A, 526, 30). Identifying such GRBs is important for constraining the fraction of obscured star formation. In both cases, NIR emission is expected. X-shooter can adequately study these objects, provided that a NIR counterpart is timely identified, for which we have the dedicated HAWKI run D.

The detection of **absorption line variability** can reveal the burst influence on the surrounding medium and in turn the ab-

sorber distance from the burst and its metallicity (Vreeswijk et al. 2007, A&A 468, 83; D'Elia et al. 2009, ApJ, 694, 332; Thöne et al. 2011, MNRAS, 414, 479; De Cia et al. 2012, A&A, 545, 64; Hartoog et al. 2013). **Short GRBs** originate in a substantially different environment compared to long GRBs. Short GRBs may be related to the merging of compact binaries and the coalescence time can be long enough to allow the progenitor system to move far away from the star formation site (Belczynski et al. 2002, ApJ, 571, 147). Up to now, however, no spectrum with a sufficient signal-to-noise ratio of a short GRB afterglow has been secured. A knowledge of the redshift distribution of short bursts is of key importance for the next generation of gravitational wave experiments, as they are the likely EM counterparts to their primary targets.

2. Sample selection criteria

2.1. Sample selection criteria

Being of transient nature, it is difficult to impose strong sample selection criteria on GRBs, without hampering the follow-up effort. Many natural follow-up restrictions exists from already, being it weather conditions, pointing restrictions of the telescope or poorly localized bursts as reported by the *Swift*-telescope. To maximize the return of the follow-up campaign we have chosen a few selection criteria that attempts to provide an unbiased selection of bursts, while allowing for a high success-rate [1]

1. GRB triggered onboard by Swift.
2. Galactic $A_V \lesssim 0.5$ mag.
3. XRT started observing within 10 minutes since the GRB; an XRT position must be distributed within 12 hr.
4. The target must be visible for at least 60 minutes at least 30 degrees above the horizon, with the Sun below -12.
5. No bright closeby stars.

A fraction of the bursts presented here (Insert exact number) have already had their hosts investigated in Krühler et al. (2015), for which extractions of the hosts exist. The focus of the data presented here are on the afterglows themselves and in the absence of a clear afterglow, the host. We will not, however, investigate the hosts.

We simultaneously want to minimize any biases against astrophysical conditions while at the same time maximizing likelihood of observations. By restricting the selection criteria to conditions local to Galaxy.

2.2. Follow-up procedure

2.2.1. RRM observations

The rapid-response mode is

3. Observations

Observations in this sample has been carried out using the cross-dispersed echelle spectrograph, X-shooter (Vernet et al. 2011), mounted on two of the four Unit Telescopes at ESO/VLT, UT2

(Kueyen) and UT3 (Melipal) during the duration of this follow-up campaign, which covers the entire lifetime of X-shooter. Observations have been carried out from the ESO period P84 through P98 under the following programme IDs: 098.A-0055, 097.A-0036, 096.A-0079, 095.A-0045, 094.A-0134, 093.A-0069, 092.A-0124, 0091.C-0934, 090.A-0088, 089.A-0067, 088.A-0051, 087.A-0055, 086.A-0073, 085.A-0009 and 084.A-0260. A few additional bursts, not a part of the *statistical sample*, have been included from 092.D-0056(A) (PI: Rau), 092.D-0633(E) (PI: Greiner), and Levan under 095.B-0811(B) (PI: Levan). This sample represents *all* GRBs that have ever been followed up by X-shooter.

The first GRB followed up is GRB090313, observed 15th of March 2009, which was while X-shooter was mounted on UT3 during the commissioning of the instrument. The bursts observed during the commissioning period is not a part of our statistical sample, but are nonetheless published as part of the bursts observed by the X-shooter GRB team. The first burst observed after science verification was completed when X-shooter was moved to UT2 is GRB091018 which thereby constitute the first burst entering our statistical sample. For all bursts that fulfill our sample selection criteria, described in Sect. 2.1, spectroscopic follow-up has been attempted with X-shooter. Various conditions can affect our ability to follow up a given burst, and a discussion of this effect is included in Sect. 5.3.

X-shooter can cover the spectral wavelength region from 3000 Å to 24800 Å in a single exposure, by splitting the light in three separate spectroscopic arms using dichroics. This way each arm work as a separate instrument, each functioning as its own echelle spectrograph. The ultraviolet blue(UVB) arm covering 3000 - 5500 Å, the visual(VIS) arm covering 5500 - 10200 Å, and the near-infrared()NIR) arm covering 10200 - 24800 Å with the possibility of applying a k-band blocking filter cutting the coverage of the NIR arm at 10200 - 21000 Å.

(ABBA)

For the large majority of the bursts we have observed with a slit width of 1″0, 0″9, and 0″9 for the UVB, VIS, and NIR-arm respectively, which puts a lower limit on the delivered resolution of the spectra based on the tabulated values of the delivered resolutions, which is 4350, 7450, and 5300 for the UVB, VIS and NIR-arm respectively[2]. The slit width also sets the width of the atmospheric sky lines and determines the amount of light lost due to the wavelength-dependent seeing PSF extending outside the coverage of the slit, where the width of sky-lines is always set by the slit width whereas both the delivered resolution and the slitloss changes for the better as the seeing PSF drops below the slit width. For atmospheric conditions delivering a seeing PSF with a FWHM of 0″9 observed with a 0″9 slit only 76.1 percent of the light will enter the slit, meaning that for almost all observations a slitloss correction is required. We describe how slitlosses were corrected for in Sect. 4.1. For accurate measurements of velocity widths, a precise instrumental resolution is required and this becomes better when the delivered seeing is better than the slit width. We discuss this in Sect. 4.5.
(ADC discussion)

We list the overview of all the observations in Tab. 1. and plot the positions off all the bursts on the night sky in Fig. 1. The central zone of avoidance due to high galactic extinction cutoff is visible with an apparent isotropic distribution of the bursts away

---

[1] Note that in the P84 proposal the criteria have been stated a bit differently, the visibility constraint being replaced by a declination + Sun angle constraint. The below criteria are however those defining the sample.

[2] https://www.eso.org/sci/facilities/paranal/instruments/xshooter/inst.html
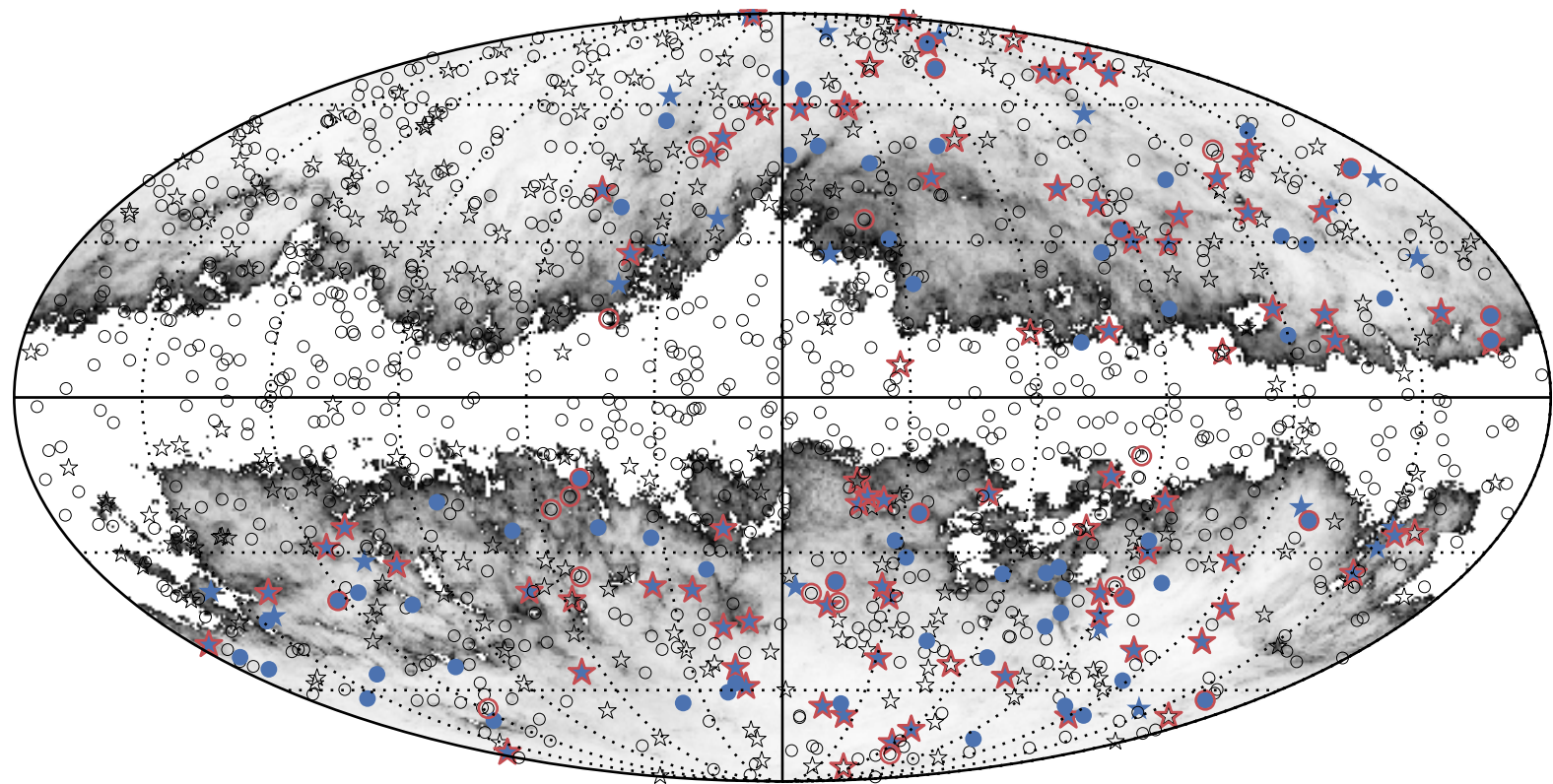
Fig. 1: Mollweide projection in galactic coordinates of the full sky showing the positions on the sky of the bursts presented in this work. The empty circles are the positions of all the *Swift* bursts detected until the end of 2016. In blue is shown the position of the bursts fulfilling the sample criteria specified in Sect. 2.1. The red circles are added around GRBs which have been followed up by X-shooter since the commissioning of the instrument. Blue points with red circles represent GRBs that enter our sample and have X-shooter spectroscopy. The different samples are compared in Sect. 5. The background shows the dust maps presented in Schlegel et al. (1998) where the sample criteria cut with $A_V \lesssim 0.5$ mag is removed.

from the galactic center except in the upper right corner, where Earth casts a shadow as seen from the telescope.

4. Data processing

In this section we describe how the final data products are produced and subsequently post-processed. All post-processing scripts developed for this dataset are made publicly available at https://github.com/jselsing/XSGRB_reduction_scripts, along with instructions of use.

Before any reductions are done, the raw object images are run through the cosmic-ray removal algorithm (van Dokkum 2001) implementation, *Astro-SCRAPPY* [3], where a wide clipping radius have been used around detected cosmics to ensure that edge residuals are robustly rejected.

The basis for the reductions is the VLT/X-shooter pipeline, version 2.7.1 or newer (Goldoni et al. 2006; Modigliani et al. 2010). The pipeline is managed with the Reflex interface

(Freudling et al. 2013) and is used for subtraction of bias level, flat-fielding, tracing of the echelle orders, wavelength calibrations with the use of arc-line lamps, flux calibration using spectrophotometric standards (Vernet et al. 2009; Hamuy et al. 1994), mirror flexure compensation, initial sky-subtraction and lastly the rectification and merging of the orders. For the initial sky-subtraction, the background has been estimated in regions adjacent to the object trace clear of contaminating sources. Because of the broken ADC, for some objects there is a lot of curvature in the object trace. This means that for some bursts, the initial sky-estimate has been made from a limited number of pixels in the spatial direction. By doing an initial subtracting the sky on the un-rectified image we ensure that bulk of the sky background is not redistributed by the rectification process.

The image is rectified onto an equidistant grid with a dispersion sampling of 0.2 Å/pixel and a 0.16 "/pixel spatial sampling for the UVB and VIS arm and 0.6 Å/pixel with a 0.21 "/pixel in the NIR arm. Because the tabulated resolution is a lower limit, by choosing a sampling of 0.2 Å/pixel, we ensure that the bluest part

---

[3] https://github.com/astropy/astroscrappy

of neither of the arms have a sampling lower than the Nyquist sampling rate of 2 pixels per resolution FWHM.

4.1. Post-processing

For a typical observation, each of the exposures in the nodding sequence has been reduced as single observation and then subsequently combined to form a single image. Because this strategy is employed, we can reject outliers in the stack and weight by the average inverse variance of the background. When weighting images where the noise in each pixel is dominated by Poisson noise it important to estimate the background variance in a large enough region, so that to remove the correlation between the signal and the weights. To this end, the weight map is generated by a running median window over the variance map, where the trace as been masked and width of the window is chosen to be wide enough for median variance to be generated on the basis of several hundred pixels. This weighting scheme automatically also optimally combines images of different exposure times or images where the background is varying, which is often the case when a burst has been observed close to twilight

Because the background is very bright and there is a high abundance of broad sky-lines in the NIR arm, when there are no contaminating sources in the slit, the sky has been put back on the images and they have been reduced in pairs of two, subtracting the two from each other, keeping the WCS static. This amounts to the regular nodding reduction, only we can reject outliers and weight by the averaged inverse variance map.

By STARE reducing all observations we additionally get a spectrum of the sky, which we can use to calibrate the wavelength solution in Sect. 4.2.

4.2. Correction for offsets in the wavelength calibration

X-shooter, being installed at the VLT Cassegrain focus is prone to flexures during operations. The flexures modify the projection of the slit on the detector with respect to the one obtained in daytime calibration. This requires a modification of the wavelength solution in order to process correctly the night-time data. Part of this correction is performed by the pipeline using the frames taken during X-shooter Active Flexure Compensation procedure [4].

The remaining offset is corrected by cross-correlation with a synthetic sky spectrum (Noll et al. 2012; Jones et al. 2013) after the continuum, estimated as the mode of all flux values, has been subtrated. To get the correct seeing PSF with which to convolve the synthetic sky an initial refinement of the wavelength solution have been obtained by cross-correlating the observed sky with an unconvolved synthetic sky. This preliminary wavelength calibration is applied to the observed sky. The synthetic spectrum is then convolved with an increasing seeing PSF and the width that minimizes χ^2 with the updated observed sky is chosen to be the effective sky-PSF. Using the synthetic sky with the matched resolution, a final wavelength calibration can then be calculated by cross-correlating the observed sky with the correctly broadened sky spectrum, as a function of a velocity offset. Both a multiplicative and an additive offset to the wavelength calibration has been tested, but in terms of χ^2, the model with only a multiplicative offset is preferred.

The resulting offsets, which were smaller than 0.1 Å in the UVB and VIS data and smaller than 0.5 Å in the NIR spectra,

but changing over short period of time were applied to the corresponding spectra.

Using the convolved synthetic sky, the $\gtrsim 3\sigma$ sky brightness pixels have been added to the bad pixel map to avoid the cores of the brightest sky-lines.

4.3. Spectral extraction

To extract the afterglow spectrum from the rectified 2D-image, several techniques have been employed based on the brightness of the afterglow and the complexity of the objects entering the slit. Due to the malfunctioning ADC, see Sect. 3, the spectral trace moves across the slit as a function of wavelength for a large fraction of the bursts observed meaning that using a single aperture for the spectral extraction is inadequate due to the large amount of background that would then enter the slit. To optimally select the extraction regions we therefore need to model the trace position.

To get the shape and the position of the spectral PSF as a function of location on the image, we need to chose a model which can represent how the light falls on the slit. We know from Trujillo et al. (2001) that the Moffat function (Moffat 1969) adequately describes an imaging PSF due to atmospheric turbulence, but due to the aberrations in the dispersion elements and the rectification process, the PSF we are trying to model different from this profile. To allow for flexibility in the model, we have chosen the Voigt function as a model for the spectral PSF and we describe how this is evaluated in App. A. Since additionally, the host galaxy could also have a contribution the image profile, this choice allows for the required freedom if additional flux is in the wings of the profile.

To guide the guess position of the trace on the slit as a function of wavelength, we have used the analytic prescription for the trace position described in Filippenko (1982), where the header keywords of the observations have been queried for the ambient conditions which controls the degree to which the trace moves.

Based on the signal-to-noise of the afterglow continuum, the 2D-image has been binned down in the spectral direction to a number of elements that allows for an accurate tracing of the PSF, typically 200 bins for moderate signal-to-noise. For each of the bins and using the guess position, the spectral PSF has been fit using the unweighted chi-squared minimization algorithm implemented in `scipy.optimize.curve_fit` (Jones et al. 2001). Since we know that the trace varies slowly as a function of wavelength, we have then fitted a low-order polynomial to the fit parameters as a function of wavelength, which allows us to evaluate the spectral PSF at all wavelengths and this way accurately model the entire spectral PSF.

Equipped with a model for how the light falls on the entire image, we can then employ the optimal extraction algorithm Horne (1986), which weights the extraction aperture by the spectral profile, or alternatively sum all pixels within 1 FWHM of the modeled profile. Where possible, we have used the optimal extraction. In cases where the trace is very weak, even in the binned images, an aperture has been selected manually which covers emission lines, if present, and when nothing is immediately visible, the entire nodding window. The error- and bad pixel maps are in all cases propagated throughout the extraction.

In cases where multiple traces are visible in the slit, additional components for the profile are used in the optimal extraction. The additional components do not share the PSF parameters and in cases where the additional component is an extended object, the fits have been inspected to ensure that the additional

---

component does now skew the fit towards a different PSF. The additional components are not used for the weights.

The spectra are corrected for galactic extinction using the E(B-V) value from the dust maps of Schlegel et al. (1998) with the update in Schlafly & Finkbeiner (2011)[5], and the extinction curve by Cardelli et al. (1989) with a total to selective extinction $R_V = 3.1$. The wavelengths of the extracted 1D-spectra are moved to vacuum, moved to the barycentric frame, and the wavelength recalibration described in Sect. 4.2 is applied. Pixels with pixel-to-pixel variation large than 50σ are added to the bad pixel map.

4.4. Telluric correction

For all earth-based telescopes, the light of interest has to pass through Earths atmosphere, where the atmospheric content and conditions make an imprint on the received spectrum. These telluric features can be calculated in a multitude of ways and we employ a prioritized list of methods here, depending on the availability of the different method. Since the observation are often taken at odd times under varying conditions, this prioritized list ensures that we are always doing the optimal correction.

The highest priority method is using the GRB afterglow continuum itself, where the atmospheric conditions have directly been imprinted on the spectrum. The telluric features can directly be fit with an atmospheric model (Smette et al. 2015; Kausch et al. 2015), which can then be used to correct for the absorption. The accuracy of the correction depends on the The requirement here is that the afterglow continuum spectrum has a signal-to-noise higher than a value of 10.

If the afterglow is not sufficiently bright, telluric standard stars observed close in the time to the GRB can be used as a proxy for the atmospheric condition during the GRB observation. Here we employ the telluric correction method that has been developed in Selsing et al. (2015), where a library of synthetic templates is fit to the observed telluric standard.

In the last case, where the object is neither bright enough, or there for some reason have not been observed a telluric standard, we rely on the synthetic sky model by (Noll et al. 2012; Jones et al. 2013) for which we generate a synthetic transmission spectrum, which we then use, where the ambient parameters for the observations have been used.

4.5. Spectral resolution

The afterglow spectra described in this paper are obtained in Target-of-Opportunity (override) mode. In most cases there is therefore little possibility to tweak slit widths to the seeing at the time of observations (i.e. to optimise spectral resolution and signal to noise), and almost all our data is therefore taken with a fixed set of slit widths and binning, described above. In a fair number of cases, the seeing full width at half maximum (FWHM) is considerably smaller than the silt width, and the delivered spectral resolution will then be determined by the seeing rather than slit width, as afterglows are point sources (this is evidently not the case for extended sources, e.g for host galaxies). The delivered resolution for slit width dominated spectra post-reduction and extraction can easily be determined from the bright sky emission lines. For afterglow spectra with very high signal to noise, the delivered spectral resolution can at times be determined from the science data themselves. However, in the
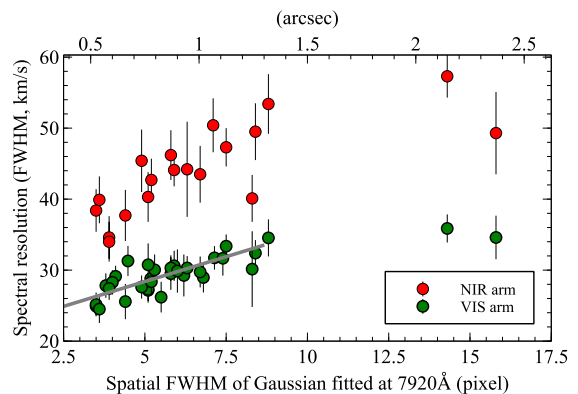
Fig. 2: Green datapoints show the FWHM (km/s) of Gaussian fits to unresolved telluric absorption lines in the VIS spectra, as a function of the FWHM of a Gaussian fit onto the trace in spatial direction at 792 nm. The lower horizontal axis is in units pixels, the top axis in arc seconds. The red datapoints show a subsample of NIR spectra. The grey line shows a linear fit to the VIS datapoints.

presence of multiple velocity components in absorption, other forms of line broadening, and a lack of lines at some redshifts, this is difficult to do at poorer signal to noise ratios (the majority of spectra in our sample). A broad starting value for the expect resolution will help fitting of these spectra, and can be important in upper limit determination, and for this reason we construct a aim to construct a crude relation between the seeing and the delivered resolution at our slit width, binning, and reduction pipeline settings. To this end we use observations of telluric standard stars that are taken with identical instrument settings as our afterglow spectra, usually just after the science data, as part of the ESO X-shooter calibration plan. These spectra have been reduced together with the afterglow spectra, using identical pipeline settings with the same version of the pipeline. First we fit a Gaussian function in the spatial direction of the trace of the standard star at 792 nm (i.e. in the VIS arm). After this, we fit a series of 20 telluric absorption lines in the telluric standard star spectra with Gaussians, taking care to select transitions that are not almost-resolved multiples, should be intrinsically unresolved, and are in areas with well defined continuum flux. We pick 34 telluric standard stars spanning a range of DIMM seeing values, with the majority between $0.5 - 1.5 arcsec$. The resulting distribution of spectral FWHM (km/s) as a function of spatial FWHM at 792 nm is fairly well described by a linear relation $a + b * x$, with x the spatial FWHM in pixels (with 0.15 arc sec per pixel), $a = 21.4 \pm 1.3$ km/s, $b = 1.4 \pm 0.2$. We use this linear relation as a way to estimate the spectral resolution for medium to poor signal to noise afterglow spectra in the VIS arm. To extend this to the UVB and NIR arm, we measured a series of lines in NIR arm spectra of a subset of 19 sources used for the VIS arm above, and find that the resulting distribution is consistent with a simple scaling of the VIS arm relation by the ratio of resolutions of the NIR and VIS arm for unresolved, slit filling, sources as given on the ESO instrument website. The UVB arm contains no suitable absorption lines to use, and we therefore use a scaled value as in the NIR arm. While this simple method is not terribly accurate (for one, the spatial profile of the trace is not a perfect Gaussian), but it gives a sufficiently accurate estimate for the analysis of these poor signal to noise science spectra.
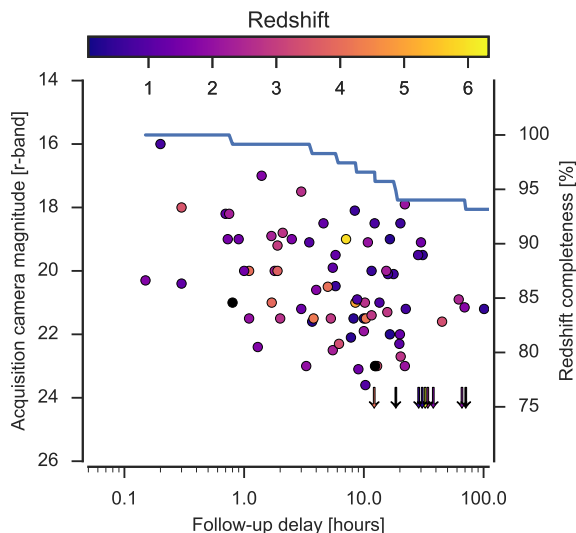
Fig. 3: Follow-up timing and afterglow magnitude at the start of observation. The points have been colored based on the redshift of the corresponding burst. Points with black faces does not have a redshift determination and downarrows indicate a non-detection in the acquisition image. In blue is shown the fractional redshift completess as a function of delay-time.

5. Results

In this section we describe the efficiency of the follow-up effort and the characteristics of the observed bursts. We also assess the degree to which the sample obtained is complete. An important note is that here we present *all* GRBs that have ever been observed with X-shooter, while only a subset of these constitute our *statistical* sample. The statistical sample is based on the selection criteria described in Sect. 2.1 and should represent an unbiased sample of the underlying, parent GRB population. Single bursts outside the sample criteria have been followed up on the basis of the curiosity of their light curve or their brightness, but is not discussed as part of the investigation of the GRB population. A prime example of a burst outside the statistical sample is GRB161023A with it's rich spectrum containing 11 intervening absorption systems and pending further analysis.

5.1. Follow-up timing and afterglow brightness

Redshift determination of bursts where the host is too faint for a spectroscopic redshift relies on the absorption spectrum imprinted on the GRB afterglow continuum, which again depends on the afterglow brightness at time of follow-up. Because the afterglow rapidly fades (Nousek et al. 2006; Vecchio et al. 2016)(Better references) a rapid follow-up is essential for the accurate designation of the GRB host (Get reference). In Fig. 3 we plot the follow-up delay from the BAT trigger to the start of the spectroscopic observation. Visible as the shortest delays are the bursts observed in RRM-mode in which where the fastest follow-up between BAT trigger and start of spectroscopic observations is for the short, $z = 1.717$, GRB160410A which was followed up only 8.4 minutes after the BAT trigger.

To illustrate the effect of redshift completeness loss due to late follow-up, we overplot the redshift completeness fraction over the delay time. Visible is the increasing fraction of GRBs

without a good redshift determination for increasing delays. That the redshift completeness of the bursts we have followed up are > 90 percent (Get number), shows the ability of VLT/X-shooter to successfully get redshifts. Not shown in the figure is an additional 12 (Get number) bursts that we have redshift determinations from late-time host observations with delay-times longer than ~10 days.

5.2. Sample completeness

Based on the sample criteria specified in Sect. 2.1, a total of 158 (Get number) bursts has been triggered by *Swift* in the period since the commissioning of VLT/X-shooter in (Insert date). This sample constitutes the *statistical sample* on which we will try to address the GRB population properties. Of this sample, 86 (Get number) have been spectroscopically followed up with X-shooter. In order to assess whether our sample criteria and the subset of bursts followed up represent the underlying parent population of GRB, we compare some intrinsic GRB properties of our sample to the full sample of GRBs followed up by *Swift*. Under the assumption that *Swift* randomly samples the underlying GRB population, if the sample statistics of our subsample are similar to the *Swift*-sample, we can assume that the population properties should be conserved. There is some evidence that the burst duration does not scale with redshift as expected through time-dilation(Kocevski & Petrosian 2013; Littlejohns et al. 2013), pointing towards that we could be missing an increasing fraction of the bursts at higher redshifts, but Lien et al. (2016) argues that we should only be missing the bright "short" GRBs", but to the degree that *Swift* is complete, we can test if the sample presented here is complete. We show the comparison between the burst properties in Fig. 4.

Using the observational characteristics of the 1244 (Get number) bursts observed by *Swift* to date Gehrels et al. (2009), and the X-ray derived hydrogen column densities (Evans et al. 2009), we can quantify the degree to which our sample is biased against the overall *Swift* sample in terms of intrinsic GRB properties. The values are queried from the online *Swift* database maintained[6]. Three main samples are of interest to compare to assess the completeness of the follow-up campaign; the full *Swift* sample consisting of all the bursts observed by *Swift* (1), the burst that fulfill the selection criteria imposed in Sect. 2.1 (2), and the bursts actually followed up with X-shooter (3).

For each of the samples we calculate the median and 14th and 86th percentile which can be used as point estimates for the population distribution. These are shown in 2. It can be seen from the values that the three samples have very similar distributions in terms of the point estimates chosen, suggesting that our selection criteria are unbiasing against the *Swift*-sample and that additionally, the follow-up effort is unbiasing towards the intrinsic GRB properties. This is despite spectroscopic follow-up only being carried out in cases where either a detectable optical afterglow or a clear counterpart are seen, which naively should be biased against dark bursts occurring in more obscured galaxies, which is shown to exhibit different galactic properties (Perley et al. 2009; Krühler et al. 2011; Rossi et al. 2012; Perley et al. 2013, 2015).

Additionally, using a 2-sided Kolmogorov-Smirnov test (KS-test), we can assess the degree to which the null that the two distribution are drawn from the same distribution can be rejected. We show a graphic representation of the test statistics in Fig. 5. We have run the test on whether is can be rejected that the

---

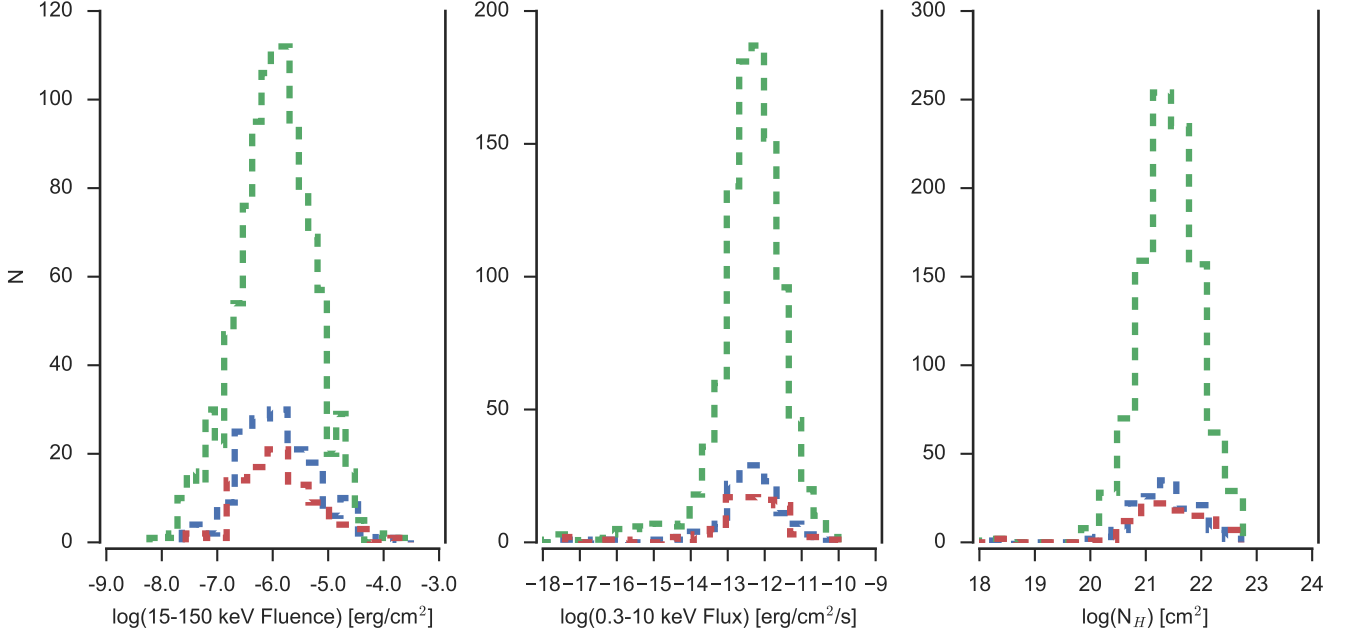[6] http://swift.gsfc.nasa.gov/archive/grb_table/

Fig. 4: Comparison between bursts properties of all bursts observed with *Swift*, the properties of the ones that fullfill the sample criteria specified in Sect. 2.1, and the subset that has been observed as part of the statistical sample. The left plot shows the fluence in 15-150 keV as observed by BAT. The middle panel shows the 0.3 - 10 keV flux, 11 hours after the bursts as measured by XRT. Based on the XRT spectrum, (Evans et al. 2009), a hydrogen column density has been inferred which we show in the right most panel.

	Full *Swift* sample	Statistical sample	Followed up bursts
N_{BAT}	1071	156	85
$\log(15-150 \text{keV fluence})$	$-5.9^{+0.6}_{-0.7}$	$-5.9^{+0.7}_{-0.6}$	$-5.9^{+0.7}_{-0.6}$
N_{XRT}	1004	154	84
$\log(0.3-10 \text{keV flux})$	$-12.3^{+0.7}_{-0.8}$	$-12.4^{+0.7}_{-0.8}$	$-12.4^{+0.8}_{-0.6}$
N_{HI}	1034	155	85
$\log(N_H)$	$21.4^{+0.5}_{-0.5}$	$-21.3^{+0.6}_{-0.6}$	$21.4^{+0.7}_{-0.7}$

Table 2: Population properties for the *Swift sample* and the subset of bursts fulfilling the sample criteria. The population characteristics for the three samples exhibit a large degree of similarity, signifying the ability of our selection criteria to effectively capture the underlying population.

sample criteria is drawn from the same distribution as the *Swift* sample, if the observed sample is dissimilar from the statistical sample, and again whether the observed sample differs from the full *Swift* sample. A high p-value indicates little evidence against the null meaning for the parameters investigated here, only the X-ray derived column densities exhibits the highest degree of dissimilarity, but not to a significant level. A large part of the tension between the two samples in N_H is driven by a small number of low column densities($\log(N_H) \lesssim 19 \text{cm}^2$) bursts.

We therefore conclude that the sample presented here, to a high degree represents the intrinsic properties of the GRBs in the full *Swift* sample.
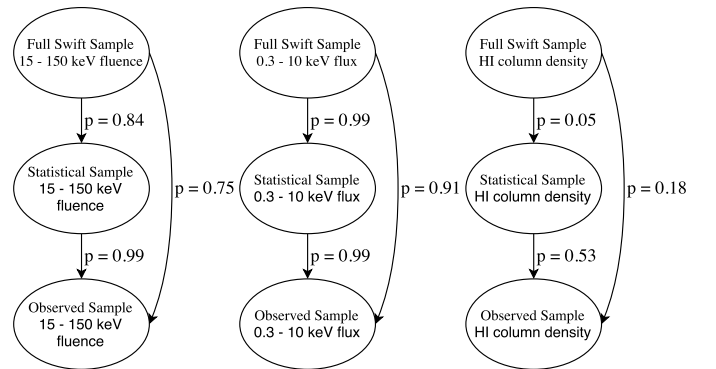
5.3. Properties of rejected triggers

GRB follow-up requires the immediate availability of the telescope in order to successfully carry out spectroscopic observations. Out of the 158 (Get exact number) bursts in the statistical sample, 32($\sim$ 20 percent) (Get exact number) have not been

Fig. 5: Relational graph shown the .

observed due to conditions, not relating the GRB or afterglow properties. The reasons includes unavailability of the telescope due to technical maintenance such af mirror re-coating, a visi-

tor rejecting the TOO trigger, or bad weather at the observing site. Because this cut is irrespective of the GRB properties, it is not expected that this should change sample properties. Addressing whether this cut introduces a bias in the followed sample is not trivial, but in terms of intrinsic GRB properties, the sample distributions does not change by much, as shown in Sect. 5.2. (Should this be quantified somehow?)

5.4. The nature of triggered GRBs without detected optical afterglow.

A subset of all GRBs exhibit no detectable or very faint optical afterglow (Groot et al. 1998; Djorgovski et al. 2001; Fynbo et al. 2001), which had been parametrized in term of "darkness" (Jakobsson et al. 2004; van der Horst et al. 2009). The X-ray properties of this subset has previously been investigated (De Pasquale et al. 2003; Melandri et al. 2012), finding a slightly higher X-ray luminosity compared to the optically brights bursts combined with similar prompt characteristics. This indicates along with investigations of host galaxy extinction (Greiner et al. 2011; Krühler et al. 2011; Hjorth et al. 2012), that the extinction of the optical afterglow is primarily driven by the presence of dust, local to the burst (Local dust reference).

Because we only follow up targets with either a clear afterglow or counterpart, correctly associating a galaxy with a burst when there is no optical afterglow is more difficult.

This should include observations where the acquisition image has been taken, but observations were discontinued due to non-detection. What are the X-ray properties of these bursts?

5.5. On the redshift distribution of GRBs

Because the redshift completeness of our statistical sample is 54 percent (Get number), making inference of the underlying redshift distribution of GRBs is difficult. Because a large fraction of the bursts for which we were unable to secure a redshift are missing due to terrestrial reasons, see Sect. 5.3, imposing additional unbiasing cuts on the sample can increase the redshift completeness at the cost of sample size. As long as the cuts we impose are not selective in terms of the burst properties, the sample properties stay the same. The first cut we try is telescope availability such as bad weather, visitor rejected the TOO, or unavailability of the instrument. Because telescope availability is independent on the burst properties, by cutting away these from our sample, the underlying redshift distribution should be conserved. By trimming away the 30 bursts (Get number) that can be rejected due to telescope availability, the redshift completeness increases to 63 percent (Get number). As is shown in Sect. 5.1, the redshift completeness decreases with increasing follow-up delay, we can additionally increase the redshift completeness by imposing cuts on the follow-up delay. Our ability to rapidly follow up a burst is also not dependent on the burst properties and therefore we can additionally cut delays longer than 24 hours (all burst in the sample are in principle observable within 24 hours).

5.6. Redshifts

The biased introduced in the redshift distribution by the increased ability to secure redshift of optically brighter bursts has been investigated by Turpin et al. (2016) which find that we systematically find redshift for longer GRBs. Additionally only the brightest GRBs are seen above redshift $z \gtrsim 1$. (Additional text)
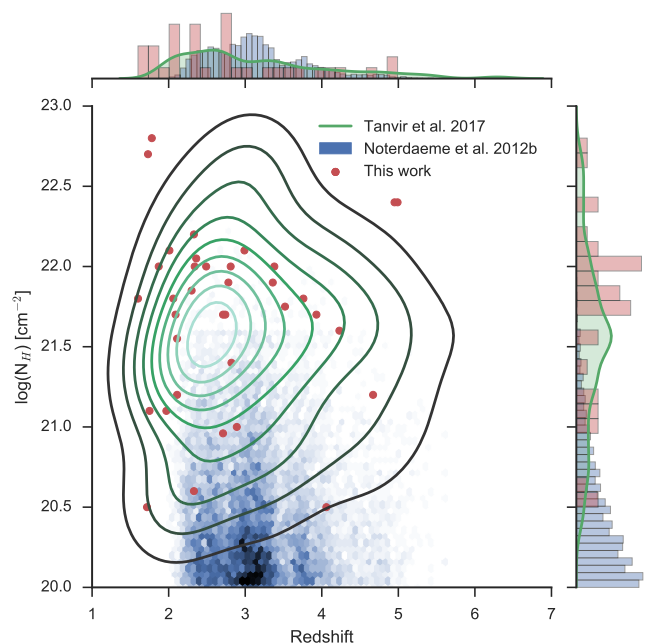
Fig. 6: Distributions of DLA hydrogen column densities for DLAs found in quasar absorption lines, from (Noterdaeme et al. 2012) in blue. Overplot in green is the kernel density estimate is the similar distribution, only for DLAs in GRB sightlines. Values are taken from the compilation in Tanvir2017 et al. (in prep)**?**, along with the new values presented in this sample. The marginal distributions for the two distribution are also shown, where the different environments probed are clearly visible in the hydrogen column densities, as previously also noted in Fynbo et al. (2009)

5.6.1. Afterglow-based redshifts

5.6.2. Emissionline-based redshifts

Redshift completeness

5.7. Hydrogen column densities

Because the locations of GRBs are associated with the most intensely starforming regions (Hogg & Fruchter 1999; Bloom et al. 2002; Fruchter et al. 2006), the GRB afterglow light has to propagate through the large amounts of hydrogen fueling the star formation. Because a significant fraction of the hydrogen has not been ionized yet, the optical depth at the wavelength of Lyα is very high, saturating at the line center. This causes a strong absorption system to appear in the afterglow continuum. For bursts with $z \gtrsim 1.7$, the position of Lyα moves into the spectroscopic coverage of X-shooter, meaning that we are able to detect this absorption trough due to Lyα.

Due of the stochastic nature of the Lyα-forest, the blue wing of the Lyman alpha absorption line is randomly superposed with forest systems, along with strong absorption from Mn II and Si III, making it notoriously difficult to model. Additionally, Similarly so, the red wing has got the ISM signatures imprinted on it, especially strong absorption due to Si II, [S II] and [N V] which can exhibit significant velocity structure. Along with instrumental effects, the generative model for the data that we would use in a likelihood-based analysis would be almost boundless in complexity, making formal fitting of the column densities outside the scope of this paper.

Using an analytic approximation to an absorption line profile and it's dependence on the column density (Tepper García 2006), we overplot a synthetic absorption line with a specified column density on our observed spectrum. By tuning the value of the hydrogen column density until the synthetic absorption line matches the spectrum, we can thereby infer the actual column density of the GRB sight line in a manual way. In a similar fashion, the errors on the hydrogen column can be inferred. We show the results of this procedure for all bursts where possible in Fig. 7 and the inferred hydrogen column densities in Tab. 3

Table 3: Hydrogen column densities for all bursts exhibiting Lyα absorption in the spectral coverage of X-shooter. Corresponding fits are shown in Fig. 7.

GRB	Hydrogen Column
GRB 090809A	21.7 ± 0.2
GRB 090926A	21.55 ± 0.10
GRB 100219A	21.20 ± 0.20
GRB 100425A	21.10 ± 0.20
GRB 100728B	21.2 ± 0.5
GRB 110128A	22.00 ± 0.15
GRB 110818A	21.9 ± 0.4
GRB 111008A	22.40 ± 0.10
GRB 111107A	21.0 ± 0.2
GRB 120119A	22.7 ± 0.2
GRB 120327A	22.0 ± 0.15
GRB 120404A	20.7 ± 0.3
GRB 120712A	19.95 ± 0.15
GRB 120716A	22.00 ± 0.15
GRB 120815A	22.05 ± 0.10
GRB 120909A	21.70 ± 0.10
GRB 121024A	21.85 ± 0.10
GRB 121027A	22.8 ± 0.3
GRB 121201A[a]	22.0 ± 0.3
GRB 121229A	21.7 ± 0.2
GRB 130408A	21.8 ± 0.1
GRB 130427B	21.9 ± 0.3
GRB 130606A	19.91 ± 0.02
GRB 130612A	22.1 ± 0.2
GRB 131011A	22.0 ± 0.3
GRB 131117A	20.0 ± 0.3
GRB 140311A	22.40 ± 0.15
GRB 140430A	21.8 ± 0.3
GRB 140515A	19.0 +- 0.5
GRB 140614A	21.6 ± 0.3
GRB 141028A	20.6 ± 0.15
GRB 141109A	22.1 ± 0.1
GRB 150206A	21.7 ± 0.4
GRB 150403A	21.8 ± 0.2
GRB 150915A[a]	21.2 ± 0.3
GRB 151021A	22.2 ± 0.2
GRB 151027B	20.5 ± 0.2
GRB 160203A	21.75 ± 0.10
GRB 160410A[b]	21.2 ± 0.2
GRB 161014A	21.4 ± 0.3
GRB 161023A	20.96 ± 0.05

Notes. [a] Has Lyα emission in the trough. [b] Short burst.

In a similar manner to how the X-ray derived column densities was used to assess the sample completeness in Sect. 5.2, we addresses the same question in terms of the optically derived

hydrogen column densities. Using the compilation by ? we have all 81 published HI values previously, we can compare to the 39 new HI columns added by this sample. We note that this sample increase the number of optically derived hydrogen column densities with ∼ 50 percent. We compare the median, the 14th, and 86th percentiles of the two distributions where the sample presented here has $21.8^{0.3}_{0.8}$ and the rest of the litterature values has $21.5^{0.4}_{1.5}$. We see that the two distribution has a large degree of overlap due to the large width of the distributions, but find a slightly higher median value for the new sample presented here. A 2-sided KS test gets us a p-value of p = 0.006, meaning relatively large evidence against the null that the two samples are drawn from the same underlying distribution. Because the bursts that have measurements of the hydrogen column density are selected sole based on our ability to infer a column, it is difficult to make any strong conclusions about the completeness in terms of gas content. We show the comparison between the two samples in Fig. 6, where we additionally show the column-distribution for 12081 quasar DLAs published in Noterdaeme et al. (2012). The ability of the GRBs to select the highest N_H is immediately visible as is also noted previously (Prochaska et al. 2007; Fynbo et al. 2009). The reason for this is the selection of sight lines as random position of the QSO DLAs whereas the GRB forms in dense regions in the host. The N_H distribution has also be used the infer the position of the gas in host Buchner et al. (2016) where a galaxy-wide gas reservoir is preferred.

6. Discussion

6.1. Comparison to previous samples.

This should also include a discussion of dark bursts. Cuchiara. BAT6 (Salvaterra), TOUGH

6.2. Why is the HI column truncated?

What is the expected transmission for a high-column HI, where the hydrogen primarily will be in the form of H2? Number of bursts with detected H2 and their HI column density. Rahmati Schaye, Krongold Prochaska.

7. Conclusion

References

Abrarov S. M., Quine B. M., 2015a, J. Math. Res., 7, 44
Abrarov S. M., Quine B. M., 2015b, J. Math. Res., 7, 163
Benner D. C., Rinsland C. P., Devi V. M., Smith M. A. H., Atkins D., 1995, JQSRT, 53, 705
Bloom J. S., Kulkarni S. R., Djorgovski S. G., 2002, AJ, 123, 1111
Buchner J., Schulze S., Bauer F. E., 2016, MNRAS, p. stw2423
Bufano F., et al., 2012, ApJ, 753, 67
Cardelli J. a., Clayton G. C., Mathis J. S., 1989, ApJ, 345, 245
Cobb B. E., Bloom J. S., Perley D. A., Morgan A. N., Cenko S. B., Filippenko A. V., 2010, ApJ, 718, L150

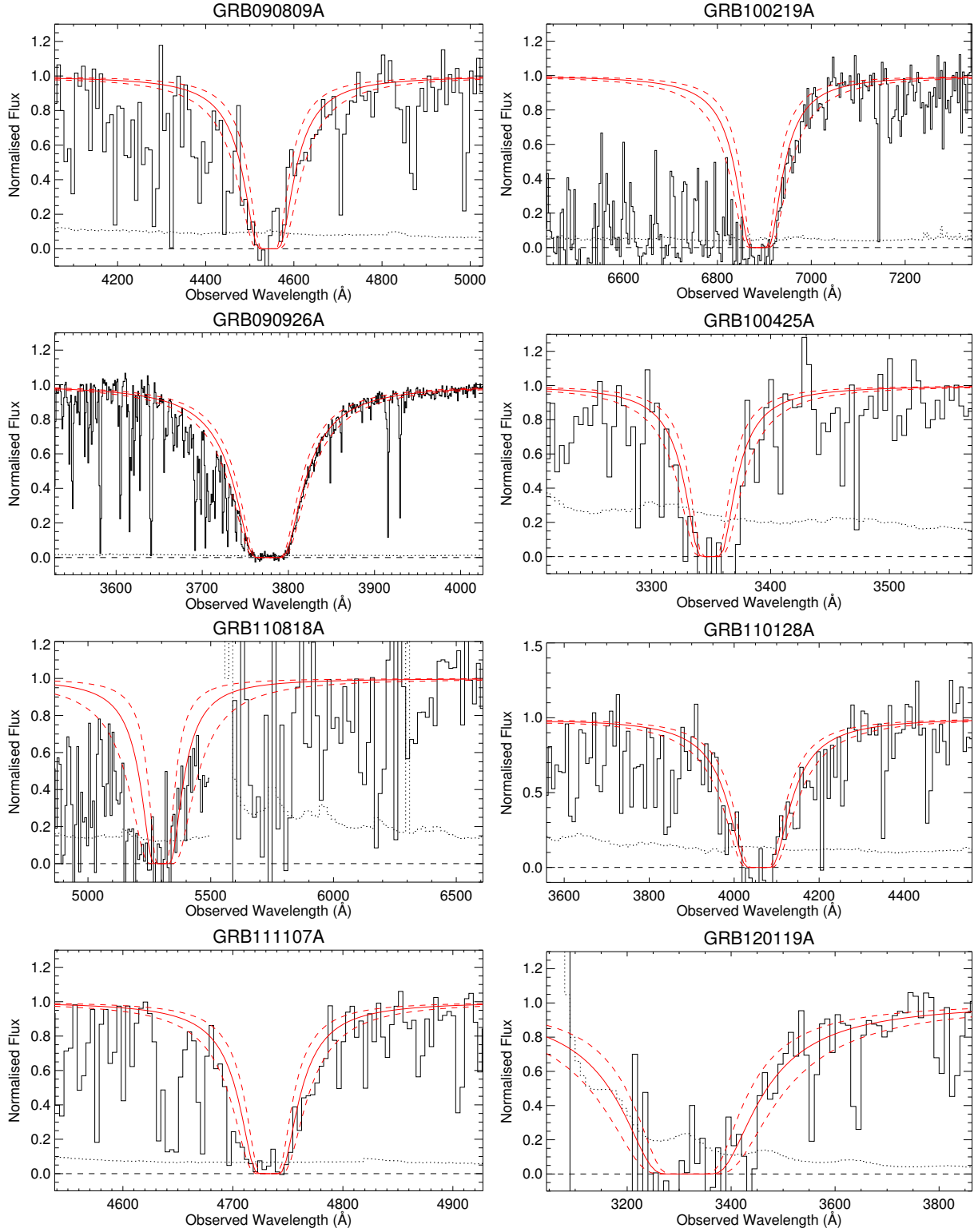Fig. 7: Measurements of the hydrogen column-densities for all bursts with a clear Lyman alpha absorption system. In solid black is shown the spectrum with black dotted giving the corresponding 1-σ error. Black dashed shows zero flux density. The solid red line is the absorption of column density equal to the value presented in Tab. **??** with the 1-σ interval shown with dashed lines.

D'Elia V., Stratta G., 2011, A&A, 532, A48
D'Elia V., et al., 2010, A&A, 523, A36
D'Elia V., et al., 2014, A&A, 564, A38
De Pasquale M., et al., 2003, ApJ, 592, 1018
De Ugarte Postigo A., Thöne C. C., Goldoni P., Fynbo J. P. U., 2011, AN, 332, 297
Djorgovski S. G., Frail D. A., Kulkarni S. R., Bloom J. S., Odewahn S. C., Diercks A., 2001, ApJ, 562, 654
Evans P. A., et al., 2009, MNRAS, 397, 1177
Filippenko A. V., 1982, PASP, 94, 715
Fong W., et al., 2013, ApJ, 769, 56
Freudling W., Romaniello M., Bramich D. M., Ballester P., Forchi V., García-Dabló C. E., Moehler S., Neeser M. J., 2013, A&A, 559, A96
Friis M., et al., 2015, MNRAS, 451, 167
Fruchter A. S., et al., 2006, Natur, 441, 463
Fynbo J. U., et al., 2001, A&A, 369, 373
Fynbo J. P. U., et al., 2009, ApJS, 185, 175
Fynbo J. P. U., et al., 2014, A&A, 12, 1
Gehrels N., Ramirez-Ruiz E., Fox D., 2009, ARA&A, 47, 567
Ginsburg A., et al., 2016, astroquery v0.3.1, doi:10.5281/ZENODO.44961, https://github.com/astropy/astroquery
Goldoni P., Royer F., François P., Horrobin M., Blanc G., Vernet J., Modigliani A., Larsen J., 2006, Ground-based Airborne Instrum. Astron. Ed. by McLean, 6269, 80
Greiner J., et al., 2011, A&A, 526, A30
Groot P. J., et al., 1998, ApJ, 493, L27
Hamuy M., Suntzeff N. B., Heathcote S. R., Walker A. R., Gigoux P., Phillips M. M., 1994, PASP, 106, 566
Hartoog O. E., et al., 2013, MNRAS, 430, 2739
Hartoog O. E., et al., 2015, A&A, 580, A139
Hjorth J., et al., 2012, ApJ, 756, 187
Hogg D. W., Fruchter A. S., 1999, ApJ, 520, 54
Horne K., 1986, PASP, 98, 609
Jakobsson P., Hjorth J., Fynbo J. P. U., Watson D., Pedersen K., Björnsson G., Gorosabel J., 2004, ApJ, 617, L21
Jakobsson P., et al., 2006, A&A, 460, L13
Jakobsson P., et al., 2012, ApJ, 752, 62
Jones E., Oliphant T., Peterson P., 2001, SciPy: Open source scientific tools for Python, http://www.scipy.org/
Jones A., Noll S., Kausch W., Szyszka C., Kimeswenger S., 2013, A&A, 560, A91
Kausch W., et al., 2015, A&A, 576, A78
Kocevski D., Petrosian V., 2013, ApJ, 765, 116
Krühler T., et al., 2011, A&A, 534, A108
Krühler T., et al., 2013, A&A, 557, A18
Krühler T., et al., 2015, A&A, 581, A125
Letchworth K. L., Benner D. C., 2007, JQSRT, 107, 173
Levan A. J., et al., 2014, ApJ, 781, 13
Lien A., et al., 2016, ApJ, 829, 7
Littlejohns O. M., Tanvir N. R., Willingale R., Evans P. A., O'Brien P. T., Levan A. J., 2013, MNRAS, 436, 3640
McGuire J. T. W., et al., 2016, ApJ, 825, 135
Melandri A., et al., 2012, MNRAS, 421, 1265
Modigliani A., et al., 2010, SPIE Astron. Telesc. + Instrum., 7737, 773728
Moffat A. F. J., 1969, A&A, 3, 455
Noll S., Kausch W., Barden M., Jones A. M., Szyszka C., Kimeswenger S., Vinther J., 2012, A&A, 543, A92
Noterdaeme P., et al., 2012, A&A, 547, L1
Nousek J. A., et al., 2006, ApJ, 642, 389
Pagnini G., Mainardi F., 2010, JCoAM, 233, 1590
Perley D. A., et al., 2009, AJ, 138, 1690
Perley D. A., et al., 2013, ApJ, 778, 128
Perley D. A., et al., 2015, ApJ, 801, 102
Perley D. A., et al., 2016, ApJ, 817, 7
Prochaska J. X., Chen H.-W., Dessauges-Zavadsky M., Bloom J. S., 2007, ApJ, 666, 267
Rafelski M., Neeleman M., Fumagalli M., Wolfe A. M., Prochaska J. X., 2014, ApJ, 782, L29
Robertson B. E., Ellis R. S., 2012, ApJ, 744, 95
Rossi A., et al., 2012, A&A, 545, A77
Salvaterra R., Campana S., Chincarini G., Tagliaferri G., Covino S., 2007, Mon. Not. R. Astron. Soc. Lett., 380, L45
Salvaterra R., et al., 2009, Natur, 461, 1258
Salvaterra R., et al., 2012, ApJ, 749, 68
Schlafly E. F., Finkbeiner D. P., 2011, ApJ, 737, 103
Schlegel D. J., Finkbeiner D. P., Davis M., 1998, ApJ, 500, 525
Schulze S., Malesani D., Cucchiara A., Tanvir N. R., Krühler T., Postigo A. D. U., Leloudas G., 2014, A&A, 102, 1
Selsing J., Fynbo J. P. U., Christensen L., Krogager J.-K., 2015, A&A, 87, 14
Smette A., et al., 2015, A&A, 576, A77
Sparre M., et al., 2011, ApJ, 735, L24
Sparre M., et al., 2014, ApJ, 785, 150
Starling R. L. C., et al., 2011, MNRAS, 411, 2792
Tanvir N. R., et al., 2009, Natur, 461, 1254
Tanvir N. R., et al., 2012, ApJ, 754, 46
Tepper García T., 2006, MNRAS, 369, 2025
Thöne C. C., et al., 2013, MNRAS, 428, 3590
Trujillo I., Aguerri J. A. L., Cepa J., Gutiérrez C. M., 2001, MNRAS, 328, 977
Turpin D., Heussaff V., Dezalay J.-P., Atteia J.-L., Klotz A., Dornic D., 2016, ApJ, 831, 28
Vecchio R. D., Dainotti M. G., Ostrowski M., 2016, ApJ, 828, 36
Vergani S. D., et al., 2011, A&A, 535, A127
Vernet J., et al., 2009, Proc. Int. Astron. Union, 5, 535
Vernet J., et al., 2011, A&A, 536, A105
Wiersema K., et al., 2012, MNRAS, 426, 2
de Ugarte Postigo A., et al., 2010, A&A, 513, A42
van Dokkum P. G., 2001, PASP, 113, 1420
van der Horst A. J., Kouveliotou C., Gehrels N., Rol E., Wijers R. A. M. J., Cannizzo J. K., Racusin J., Burrows D. N., 2009, ApJ, 699, 1087
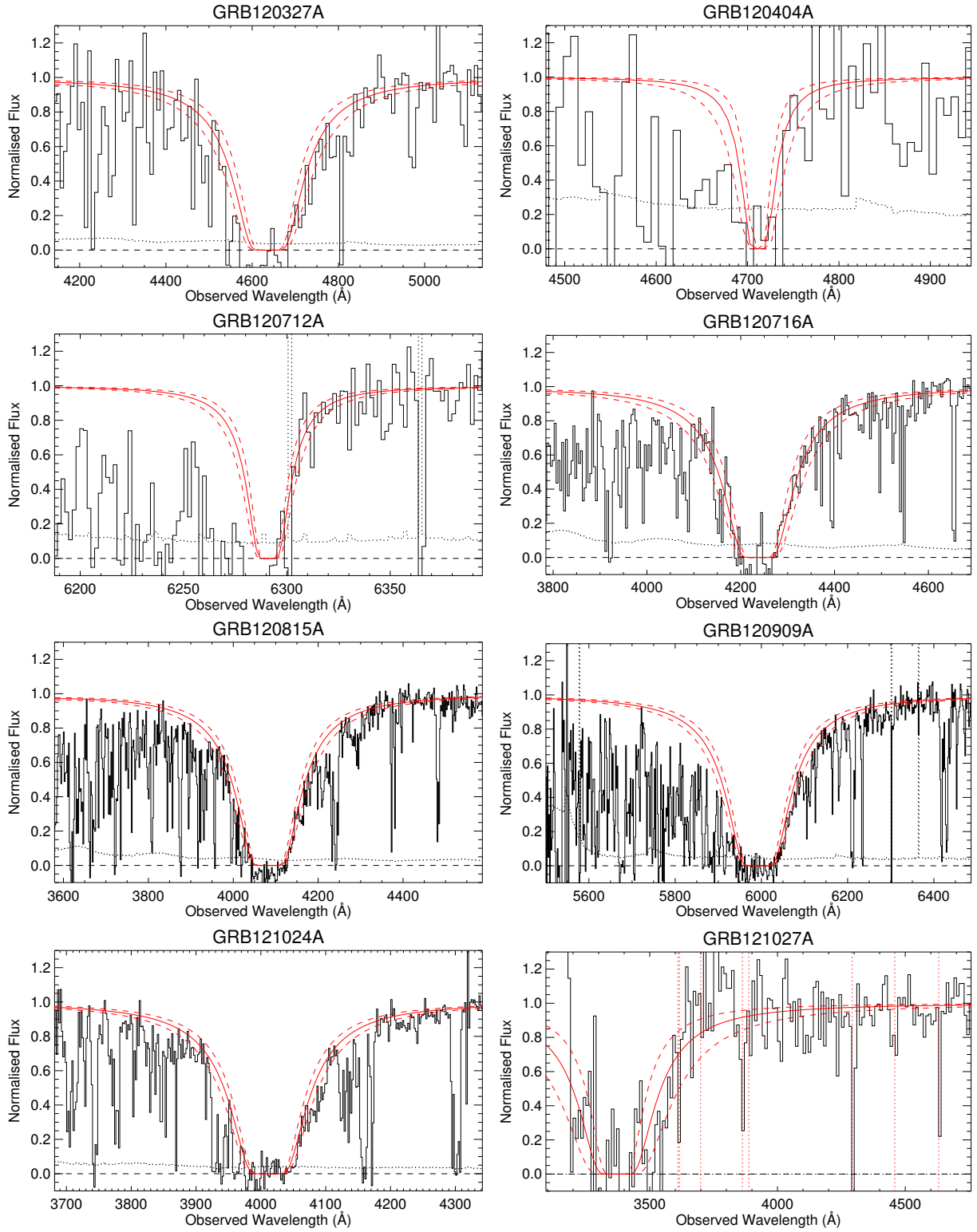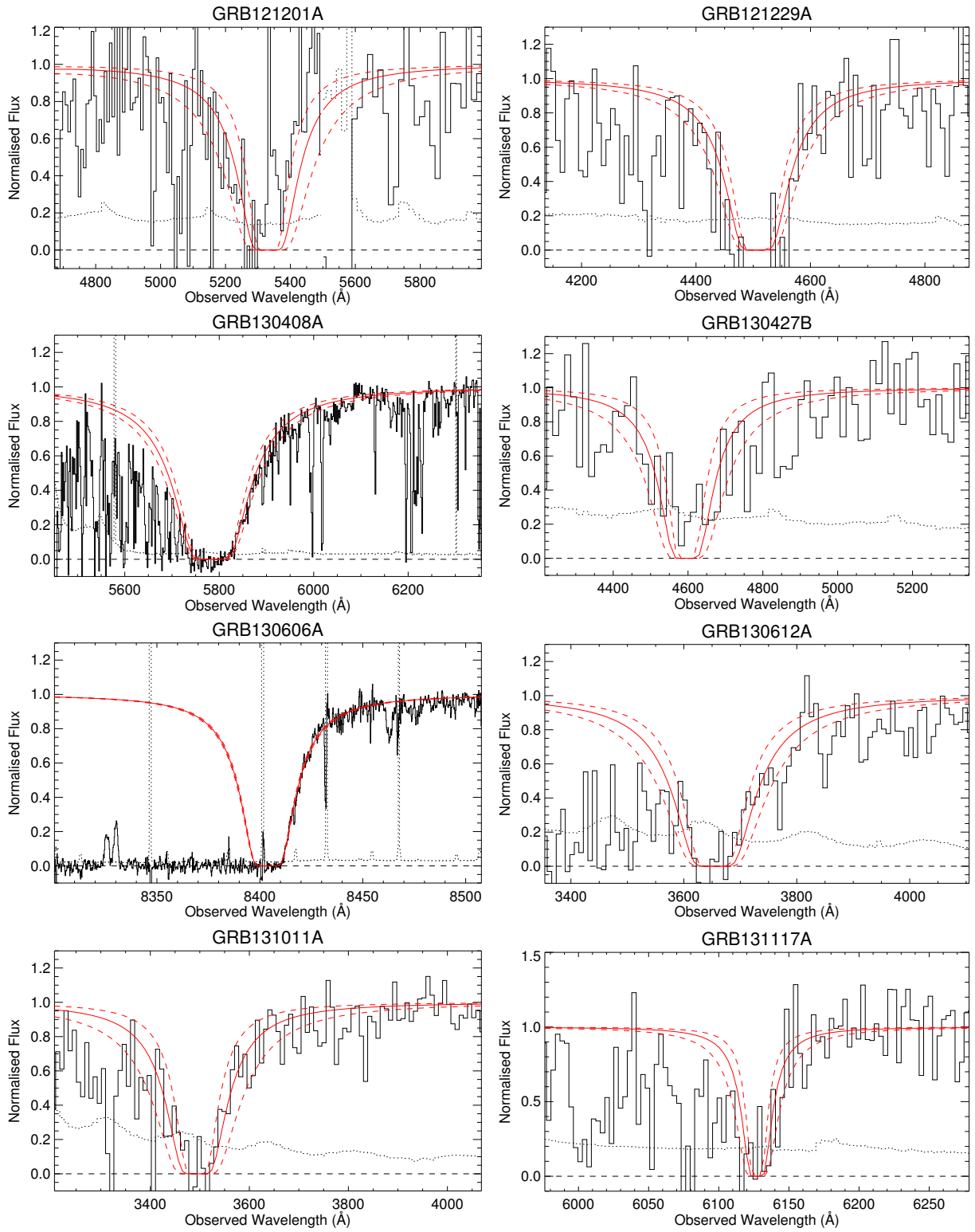
Fig. 7. continued.
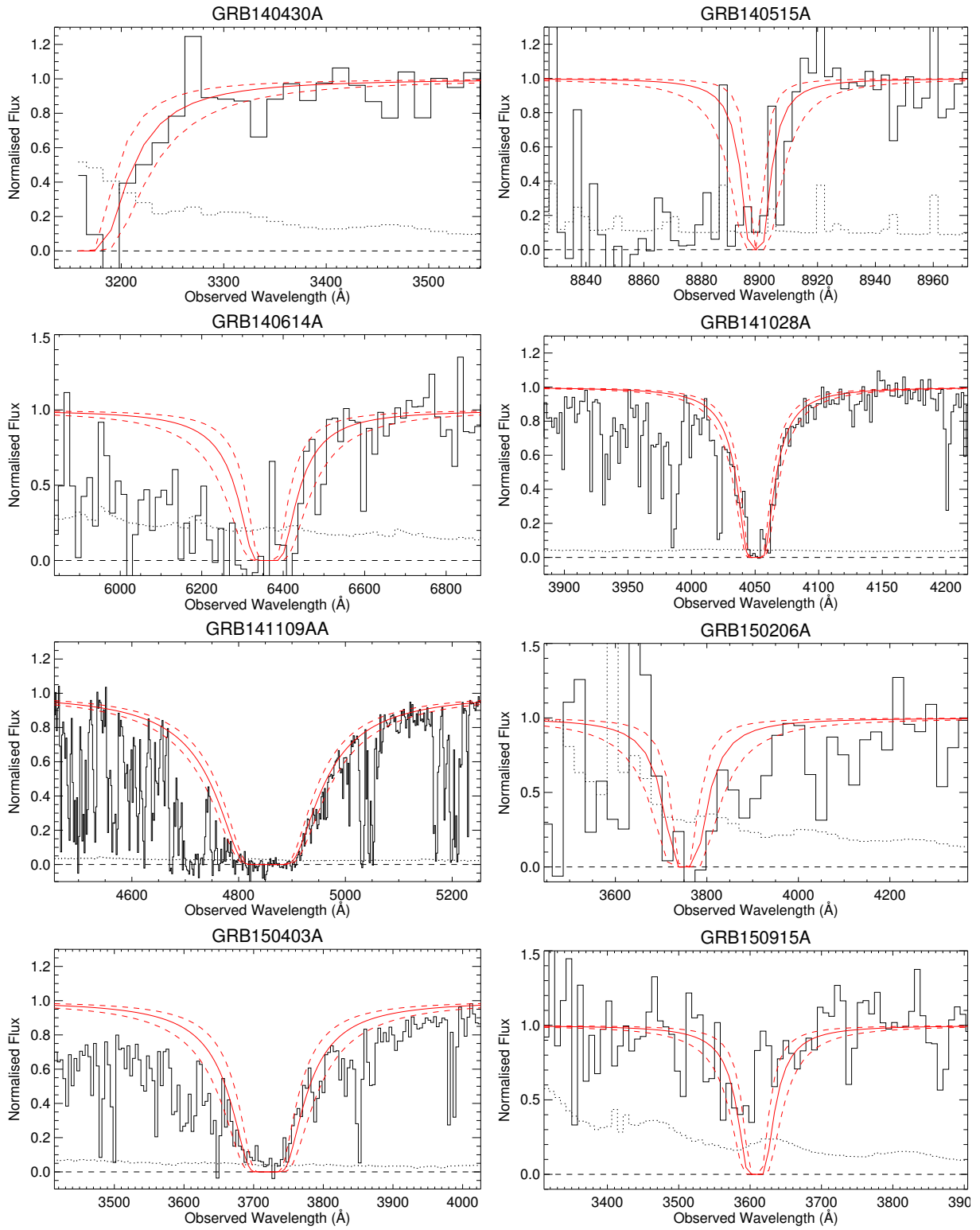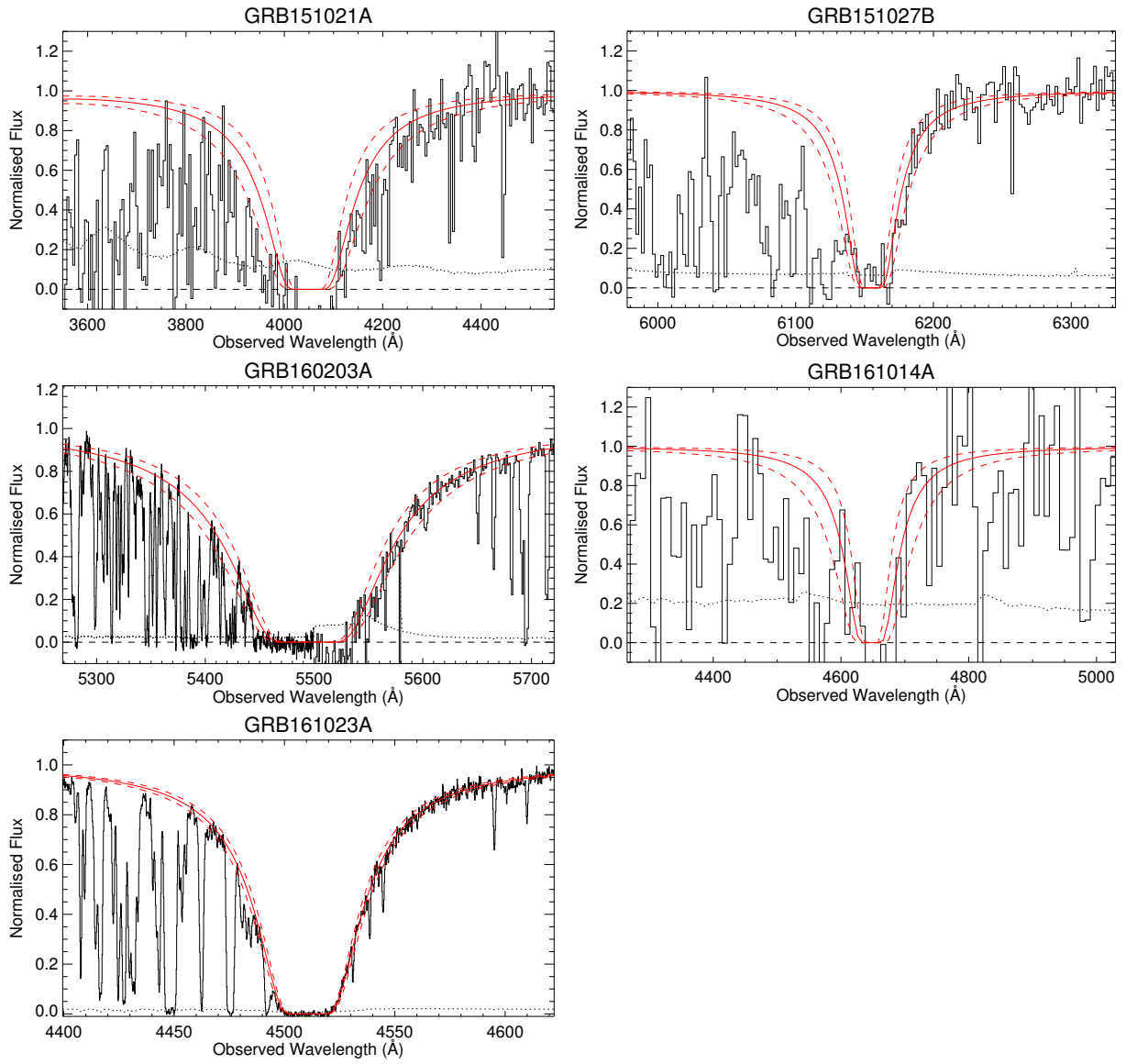
Fig. 7. continued.

Fig. 7. continued.

Fig. 7. continued.

Table 1: The full sample of afterglows or hosts observed in the program. We here list the burst names and details of the spectroscopic observations. The exposure times and slit widths are given in the order UVB/VIS/NIR. The column Δt shows the time after trigger when the spectroscopic observation was started. Mag_{acq} gives the approximate magnitude (typically in the R-band) of the afterglow in the acquisition image.

GRB	Exptime	Slit width	Airmass	Seeing	Δt	Mag_{acq}	Redshift	Ref
	(ks)	(arcsec)		(arcsec)	(hr)			
GRB090313[a]	6.9/6.9/6.9	1.0/0.9/0.9	1.2–1.4	1.0	45	21.6	3.3736	(1)
GRB090530[a]	4.8/4.8/4.8	1.0/1.2/1.2	1.6–2.2	1.5	20	22	1.266	(2)
GRB090809[a]	7.2/7.2/7.2	1.0/0.9/0.9	1.2–1.1	0.9	10.2	21	2.737	(2,3)
GRB090926[a]	7.2/7.2/7.2	1.0/0.9/0.9	1.4–1.5	0.9	22	17.9	2.1062	(4)
GRB091018	2.4/2.4/2.4	1.0/0.9/0.9	2.1–1.8	0.8	3.5	19.1	0.9710	(5)
GRB091127	6.0/6.0/6.0	1.0/0.9/0.9	1.1–1.2	1.0	101	21.2	0.490	(6)
GRB100205A	10.8/10.8/10.8	1.0/0.9/0.9	1.9–1.8	1.0	71	–	–	(2)
GRB100219A	4.8/4.8/4.8	1.0/0.9/0.9	1.3–1.1	0.7	12.5	23	4.667	(7)
GRB100316B	2.4/2.4/2.4	1.0/0.9/0.9	2.0–2.4	0.7	0.7	18.2	1.18	(2)
GRB100316D-1[b]	3.6/3.6/1.8	1.0/0.9/0.9	1.2–1.3	1.0	10	21.5	0.059	(8)
GRB100316D-2	2.4/2.4/2.4	1.0/0.9/0.9	1.1–1.2	1.0	58	20.2	0.059	(8)
GRB100316D-3	2.6/2.6/3.2	1.0/0.9/0.9	1.1–1.2	1.1	79	19.9	0.059	(8)
GRB100316D-4	2.6/2.6/3.2	1.0/0.9/0.9	1.1–1.2	1.2	101	19.9	0.059	(8)
GRB100418A-1	4.8/4.8/4.8	1.0/0.9/0.9	1.6–1.3	0.7	8.4	18.1	0.624	(9)
GRB100418A-2	4.8/4.8/4.8	1.0/0.9/0.9	1.2–1.3	0.6	34	19.2	0.624	(9)
GRB100418A-3	4.8/4.8/4.8	1.0/0.9/0.9	1.2–1.4	0.7	58	–	0.624	(9)
GRB100424A[c]	4.8/4.8/4.8	1.0/0.9/0.9	1.1–1.2	0.8	–	–	2.465	(2)
GRB100425A	2.4/2.4/2.4	1.0/0.9/0.9	1.5–1.3	0.7	4.0	20.6	1.755	(2,3)
GRB100615A[c]	4.8/4.8/4.8	1.0/0.9/0.9	1.0–1.1	0.8	–	–	1.398	(2)
GRB100621A	2.4/2.4/2.4	1.0/0.9/0.9	1.3–1.4	1.0	7.1	–	0.542	(2)
GRB100625A[c]	4.8/4.8/4.8	1.0/0.9/0.9	1.1–1.0	0.8	13	–	0.452	(2)
GRB100724A[d]	4.2/4.2/4.2	1.0/0.9/0.9	1.5–2.3	0.7	0.2	–	1.288	(2)
GRB100728B[e]	7.2/7.2/7.2	1.0/0.9/0.9	1.5–1.1	0.5	22	23	2.106	(2)
GRB100814A-1[d]	0.9/0.9/0.9	1.0/0.9/0.9	1.9–1.7	0.5	0.9	19	1.439	(2)
GRB100814A-2	4.8/4.8/2.4	1.0/0.9/0.9	1.5–1.2	0.6	2.1	19	1.439	(2)
GRB100814A-3	4.8/4.8/2.4	1.0/0.9/0.9	1.2–1.0	0.6	98	20	1.439	(2)
GRB100816A[f]	4.8/4.8/2.4	1.0/0.9/0.9	1.8–1.6	0.8	28.4	–	0.805	(2)
GRB100901A	2.4/2.4/2.4	1.0/0.9/0.9	1.5–1.5	1.5	66	–	1.408	(10)
GRB101219A	7.2/7.2/7.2	1.0/0.9/0.9	1.1–1.7	2.0	3.7	–	0.718	(2)
GRB101219B-1	4.8/4.8/4.8	1.0/0.9/0.9	1.6–2.6	1.3	11.6	20	0.552	(11)
GRB101219B-2	7.2/7.2/7.2	1.0/0.9/0.9	1.2–2.0	0.8	394	22.7	0.552	(11)
GRB101219B-3	7.2/7.2/7.2	1.0/0.9/0.9	1.4–2.1	0.9	886	–	0.552	(11)
GRB110128A	7.2/7.2/7.2	1.0/0.9/0.9	2.0–1.6	0.9	5.5	22.5	2.339	(2)
GRB110407A	9.6/9.6/9.6	1.0/0.9/0.9	1.4–1.3	2.0	12.4	23	–	(2)
GRB110709B[a c]	7.2/7.2/7.2	1.0/0.9/0.9	1.6–1.1	1.0	–	–	–	(2)
GRB110715A	0.6/0.6/0.6	1.0/0.9/0.9	1.1–1.1	1.7	12.3	18.5	0.82	(2)
GRB110721A	2.4/2.4/2.4	1.0/0.9/0.9	1.2–1.4	2.4			0.382	(2)
GRB110808A	2.4/2.4/2.4	1.0/0.9/0.9	1.2–1.1	1.1	3.0	21.2	1.3488	(2)
GRB110818A	4.8/4.8/4.8	1.0/0.9/0.9	1.3–1.3	1.0	6.2	22.3	3.36	(2)
GRB111005A[c]	1.2/1.2/1.2	1.0/0.9/0.9	1.3–1.3	0.7	–	–	0.013?	(2)
GRB111008A-1	8.8/8.8/8.4	1.0/0.9/0.9	1.1–1.0	1.2	8.5	21?	4.9898	(12)
GRB111008A-2	8.0/8.0/7.2	1.0/0.9/0.9	1.3–1.0	1.0	20.1	22?	4.9898	(12)
GRB111107A	4.8/4.8/4.8	1.0/0.9/0.9	1.8–1.5	0.7	5.3	21.5	2.893	(2)
GRB111117A[f]	4.8/4.8/4.8	1.0/0.9/0.9	1.5–1.4	0.6	38	–	1.3?	(2)
GRB111123A-1	6.2/6.6/6.6	1.0/0.9/0.9	1.6–1.1	1.0	12.2	>24	3.1516	(2)
GRB111123A-2[c]	2.4/2.4/2.4	1.0/0.9/0.9	1.0–1.0	0.5	–	–	3.1516	(2)
GRB111129A	3.6/3.6/3.6	1.0/0.9/0.9	1.6–2.1	1.7			–	(2)
GRB111209A-1	4.8/4.8/4.8	1.0/0.9/0.9	1.1–1.2	0.8	17.7	20.1	0.677	(13)
GRB111209A-2	9.6/9.6/9.6	1.0/0.9/0.9	1.2–2.0	0.8	497	23	0.677	(13)
GRB111211A[a]	2.4/2.4/2.4	1.0/0.9/0.9	1.4–1.6	0.6	31	19.5	0.478	(2)
GRB111228A	2.4/2.4/2.4	1.0/0.9/0.9	1.4–1.4	0.9	15.9	20.1	0.716	(2)
GRB120118B[c]	3.6/3.6/3.6	1.0/0.9/0.9	1.1–1.0	1.0	–	–	2.943	(2)
GRB120119A-1	2.4/2.4/2.4	1.0/0.9/0.9	1.1–1.1	0.6	1.4	17	1.728	(2)
GRB120119A-2	1.2/1.2/1.2	1.0/0.9/0.9	1.8–1.9	0.6	4.5	20	1.728	(2)
GRB120119A-3[c]	4.8/4.8/4.8	1.0/0.9/0.6JH	1.0–1.1	1.1	–	–	1.728	(2)
GRB120211A-1	4.8/4.8/4.8	1.0/0.9/0.9	1.1–1.4	1.0	–	–	2.346	(2)

Table 1: The full sample of afterglows or hosts observed in the program (continued).

GRB	Exptime (ks)	Slit width (arcsec)	Airmass	Seeing (arcsec)	Δt (hr)	Mag$_{acq}$	Redshift	Ref
GRB120211A-2	3.6/3.6/3.6	1.0/0.9/0.9	1.1–1.2	1.3	–	–	2.346	(2)
GRB120224A	2.4/2.4/2.4	1.0/0.9/0.9	1.7–2.1	1.4	19.8	22.3	1.10	(2)
GRB120311A[a]	2.4/2.4/2.4	1.0/0.9/0.9	1.6–1.4	0.6	3.7	21.6	0.350	(2)
GRB120327A-1	2.4/2.4/2.4	1.0/0.9/0.9	1.6–1.4	0.5	2.1	18.8	2.815	(14)
GRB120327A-2	4.2/4.2/4.2	1.0/0.9/0.9	1.0–1.1	1.0	29	22.5	2.815	(14)
GRB120404A	9.6/9.6/9.6	1.0/0.9/0.9JH	1.7–1.3	1.3	15.7	21.3	2.876	(2)
GRB120422A	4.8/4.8/4.8	1.0/0.9/0.9	1.3–1.3	0.6	16.5	22.0	0.283	(15)
GRB120712A	4.8/4.8/4.8	1.0/0.9/0.9	1.5–2.5	1.3	10.4	21.5	4.175	(2)
GRB120714B	4.8/4.8/4.8	1.0/0.9/0.9JH	1.5–1.2	1.2	7.8	22.1	0.398	(2)
GRB120716A[a]	3.6/3.6/3.6	1.0/0.9/0.9JH	1.8–2.6	1.0	62	20.9	2.486	(2)
GRB120722A[(b)]	4.8/4.8/4.8	1.0/0.9/0.9	1.3–1.3	1.1	10.3	23.6	0.959	(2)
GRB120805A[(b)]	3.6/3.6/3.6	1.0/0.9/0.9JH	1.3–1.7	0.9	218	–	2.8?	(2)
GRB120815A	2.4/2.4/2.4	1.0/0.9/0.9	1.3–1.4	0.6	1.69	18.9	2.358	(16)
GRB120909A	1.2/1.2/1.2	1.0/0.9/0.9	1.6–1.6	1.4	1.7	21	3.929	(2)
GRB120923A	9.6/9.6/9.6	1.0/0.9/0.9JH	1.2–1.4	1.0	18.5	–	$\geqslant 8$	(2)
GRB121024A	2.4/2.4/2.4	1.0/0.9/0.9	1.2–1.1	0.6	1.8	20	2.300	(17)
GRB121027A	8.4/8.4/8.4	1.0/0.9/0.9	1.3–1.3	0.9	69.4	21.15	1.773	(2)
GRB121201A	4.8/4.8/4.8	1.0/0.9/0.9JH	1.1–1.1	0.9	12.9	23	3.385	(2)
GRB121229A	4.8/4.8/4.8	1.0/0.9/0.9JH	1.4–1.2	1.4	2.0	21.5	2.707	(2)
GRB130131B[c]	7.2/7.2/7.2	1.0/0.9/0.9JH	1.3–1.6	0.8	–	–	2.539	(2)
GRB130408A	1.2/1.2/1.2	1.0/0.9/0.9	1.0–1.0	1.0	1.9	20	3.758	(2)
GRB130418A	1.2/1.2/1.2	1.0/0.9/0.9	1.4–1.3	1.3	4.6	18.5	1.218	(2)
GRB130427A	1.2/1.2/1.2	1.0/0.9/0.9JH	1.8–1.8	0.8	16.5	19	0.340	(18)
GRB130427B	1.2/1.2/1.2	1.0/0.9/0.9JH	1.2–1.0	0.8	20.3	22.7	2.78	(2)
GRB130603B[(f)]	2.4/2.4/2.4	1.0/0.9/0.9	1.4–1.4	1.1	8.2	21.5	0.356	(19)
GRB130606A	4.2/4.2/4.2	1.0/0.9/0.9JH	1.7–1.9	1.1	7.1	19	5.91	(20)
GRB130612A	1.2/1.2/1.2	1.0/0.9/0.9	1.3–1.3	1.4	1.1	21.5	2.006	(2)
GRB130615A	1.2/1.2/1.2	1.0/0.9/0.9	2.1–2.2	1.0	0.8	21	3?	(2)
GRB130701A	1.2/1.2/1.2	1.0/0.9/0.9JH	2.0–2.0	1.6	5.5	19.9	1.155	(2)
GRB131011A	9.9/9.9/9.9	9.9/9.9/9.9QQ	9.9–9.9				1.874	(2)
GRB131030A	9.9/9.9/9.9	9.9/9.9/9.9QQ	9.9–9.9				1.296	(2)
GRB131103A	9.9/9.9/9.9	9.9/9.9/9.9QQ	9.9–9.9		5.8	20.48	0.599	(2)
GRB131105A	9.9/9.9/9.9	9.9/9.9/9.9QQ	9.9–9.9		1.3	22.4	1.686	(2)
GRB131117A	9.9/9.9/9.9	9.9/9.9/9.9QQ	9.9–9.9		1	20	4.042	(2)
GRB131231A	9.9/9.9/9.9	9.9/9.9/9.9QQ	9.9–9.9		20.2	18.5	0.642	(2)
GRB140114A	9.9/9.9/9.9	9.9/9.9/9.9QQ	9.9–9.9				2.8	(2)
GRB140213A	9.9/9.9/9.9	9.9/9.9/9.9QQ	9.9–9.9		5.8	19.5	1.208	(2)
GRB140301A	9.9/9.9/9.9	9.9/9.9/9.9QQ	9.9–9.9		9	23.1	1.416	(2)
GRB140311A	9.9/9.9/9.9	9.9/9.9/9.9QQ	9.9–9.9				4.95	(2)
GRB140430A	9.9/9.9/9.9	9.9/9.9/9.9QQ	9.9–9.9		2.5	19	1.601	(2)
GRB140506A-1	9.9/9.9/9.9	9.9/9.9/9.9QQ	9.9–9.9		8.8	20.9	0.889	(2)
GRB140506A-2	9.9/9.9/9.9	9.9/9.9/9.9QQ	9.9–9.9		–	–	0.889	(2)
GRB140515A	9.9/9.9/9.9	9.9/9.9/9.9QQ	9.9–9.9				6.32	(2)
GRB140614A	9.9/9.9/9.9	9.9/9.9/9.9QQ	9.9–9.9		3.8	21.5	4.233	(2)
GRB140622A	9.9/9.9/9.9	9.9/9.9/9.9QQ	9.9–9.9				0.959	(2)
GRB141028A	9.9/9.9/9.9	9.9/9.9/9.9QQ	9.9–9.9		15.4	20	2.332	(2)
GRB141031A-1	9.9/9.9/9.9	9.9/9.9/9.9QQ	9.9–9.9					(2)
GRB141031A-2	9.9/9.9/9.9	9.9/9.9/9.9QQ	9.9–9.9					(2)
GRB141109A-1	9.9/9.9/9.9	9.9/9.9/9.9QQ	9.9–9.9		1.9	19.2	2.993	(2)
GRB141109A-2	9.9/9.9/9.9	9.9/9.9/9.9QQ	9.9–9.9				2.993	(2)
GRB150206A	9.9/9.9/9.9	9.9/9.9/9.9QQ	9.9–9.9		10	21.9	2.087	(2)
GRB150301B	9.9/9.9/9.9	9.9/9.9/9.9QQ	9.9–9.9				1.5169	(2)
GRB150403A	9.9/9.9/9.9	9.9/9.9/9.9QQ	9.9–9.9		10.8	19.1	2.06	(2)
GRB150423A	9.9/9.9/9.9	9.9/9.9/9.9QQ	9.9–9.9				1.394	(2)
GRB150428A	9.9/9.9/9.9	9.9/9.9/9.9QQ	9.9–9.9					(2)
GRB150514A	9.9/9.9/9.9	9.9/9.9/9.9QQ	9.9–9.9		28.4	19.5	0.807	(2)
GRB150518A	9.9/9.9/9.9	9.9/9.9/9.9QQ	9.9–9.9				0.256	(2)
GRB150616A	9.9/9.9/9.9	9.9/9.9/9.9QQ	9.9–9.9					(2)
GRB150727A	9.9/9.9/9.9	9.9/9.9/9.9QQ	9.9–9.9				0.313	(2)

Table 1: The full sample of afterglows or hosts observed in the program (continued).

GRB	Exptime	Slit width	Airmass	Seeing	Δt	Mag$_{acq}$	Redshift	Ref
	(ks)	(arcsec)		(arcsec)	(hr)			
GRB150821A	9.9/9.9/9.9	9.9/9.9/9.9QQ	9.9–9.9		0.2	16	0.755	(2)
GRB150910A	9.9/9.9/9.9	9.9/9.9/9.9QQ	9.9–9.9				1.359	(2)
GRB150915A	9.9/9.9/9.9	9.9/9.9/9.9QQ	9.9–9.9		3.3	23	1.968	(2)
GRB151021A	9.9/9.9/9.9	9.9/9.9/9.9QQ	9.9–9.9		0.75	18.2	2.33	(2)
GRB151027B	9.9/9.9/9.9	9.9/9.9/9.9QQ	9.9–9.9		5	20.5	4.063	(2)
GRB151029A	9.9/9.9/9.9	9.9/9.9/9.9QQ	9.9–9.9		1	20	1.423	(2)
GRB151031A	9.9/9.9/9.9	9.9/9.9/9.9QQ	9.9–9.9		0.3	20.4	1.167	(2)
GRB160117B	9.9/9.9/9.9	9.9/9.9/9.9QQ	9.9–9.9		13.5	21	0.87	(2)
GRB160203A	9.9/9.9/9.9	9.9/9.9/9.9QQ	9.9–9.9		0.3	18	3.52	(2)
GRB160228A	9.9/9.9/9.9	9.9/9.9/9.9QQ	9.9–9.9				1.64	(2)
GRB160303A	9.9/9.9/9.9	9.9/9.9/9.9QQ	9.9–9.9				-	(2)
GRB160314A	9.9/9.9/9.9	9.9/9.9/9.9QQ	9.9–9.9				0.726	(2)
GRB160410A	9.9/9.9/9.9	9.9/9.9/9.9QQ	9.9–9.9		0.15	20.3	1.717	(2)
GRB160425A	9.9/9.9/9.9	9.9/9.9/9.9QQ	9.9–9.9				0.555	(2)
GRB160625B	9.9/9.9/9.9	9.9/9.9/9.9QQ	9.9–9.9		30	19.1	1.406	(2)
GRB160804A-1	2.4/2.4/2.4	1.0/0.9/0.9JH	1.3–1.4	–	22.4	21.2	0.736	(2)
GRB160804A-2^c	3.6/3.6/3.6	1.0/0.9/0.9JH	1.8–1.9	–	–	–	0.736	(2)
GRB161001A	9.9/9.9/9.9	9.9/9.9/9.9QQ	9.9–9.9					(2)
GRB161007A^c	2.4/2.4/2.4	1.0/0.9/0.9JH	1.5–1.7	0.8	323	–	???	(2)
GRB161014A	4.8/4.8/4.8	1.0/0.9/0.9JH	1.1–1.2	0.6	11.6	21.4	2.823	(2)
GRB161023A	9.9/9.9/9.9	9.9/9.9/9.9QQ	9.9–9.9		3	17.5	2.710	(2)

Notes. [a] Not part of the statistical sample [b] Spectrum dominated by light from the host galaxy [c] Spectrum of the host galaxy taken long after the burst [d] RRM observation [e] ADC malfunction during observation [f] Short burst

References. (1) de Ugarte Postigo et al. (2010); (2) This work ; (3) Skuladottir (2010); (4) D'Elia et al. (2010); (5) Wiersema et al. (2012); (6) Vergani et al. (2011); Cobb et al. (2010); (7) Thöne et al. (2013); (8) Bufano et al. (2012) ; (9) De Ugarte Postigo et al. (2011) ; (10) Hartoog et al. (2013); (11) Sparre et al. (2011); (12) Sparre et al. (2014); (13) Levan et al. (2014); (14) D'Elia et al. (2014); (15) Schulze et al. (2014); (16) Krühler et al. (2013); (17) Friis et al. (2015)

Appendix A: The complex error function and the Voigt profile

When modeling the spectral PSF, we need to evaluate the Voigt-profile. The Voigt profile, which is the convolution of the Gaussian and Lorentzian profiles, can, centered at zero, be written as (Pagnini & Mainardi 2010)

$$
\begin{aligned}
V(\lambda, \sigma, \gamma) &= G(\lambda, \sigma) \otimes L(\lambda, \gamma) \\
&= \int_{-\infty}^{\infty} G(\xi, \sigma) L(\lambda - \xi, \gamma) d\xi \\
&= \int_{-\infty}^{\infty} \frac{1}{\sqrt{2\pi}\sigma} e^{-\left(\frac{\xi}{\sqrt{2}\sigma}\right)^2} \frac{1}{\gamma\pi} \frac{\gamma^2}{(\lambda - \xi)^2 + \gamma^2} d\xi \\
&= \frac{\gamma}{\sqrt{2}\sigma} \frac{1}{\pi^{3/2}} \int_{-\infty}^{\infty} \frac{e^{-\left(\frac{\xi}{\sqrt{2}\sigma}\right)^2}}{(\lambda - \xi)^2 + \gamma^2}. \quad (A.1)
\end{aligned}
$$

We can by making the following substitution, $\xi = \sqrt{2}\sigma$ and $d\xi = \sqrt{2}\sigma dt$, write it as

$$
\begin{aligned}
V(\lambda, \sigma, \gamma) &= \frac{\sqrt{2}\sigma}{\sqrt{\pi}} \frac{\frac{\gamma}{\sqrt{2}\sigma}}{\pi} \int_{-\infty}^{\infty} \frac{e^{-t^2}}{(\lambda - \sqrt{2}\sigma t)^2 + \gamma^2} dt \\
&= \frac{1}{\sqrt{2\pi}\sigma} \frac{\frac{\gamma}{\sqrt{2}\sigma}}{\pi} \int_{-\infty}^{\infty} \frac{e^{-t^2}}{\left(\frac{\lambda}{\sqrt{2}\sigma} - t\right)^2 + \left(\frac{\gamma}{\sqrt{2}\sigma}\right)^2} dt. \quad (A.2)
\end{aligned}
$$

This form of the convolution is closely related to the complex probability function (Letchworth & Benner 2007; Abrarov & Quine 2015a),

$$
W(z) = \frac{i}{\pi} \int_{-\infty}^{\infty} \frac{e^{-t^2}}{z - t} \quad (A.3)
$$

for any complex argument, $z = x + iy$. The complex probability function can be expressed as a sum of a real an imaginary part (Benner et al. 1995; Abrarov & Quine 2015b),

$$
\begin{aligned}
W(x, y) &= K(x, y) + iL(x, y) \\
&= \frac{y}{\pi} \int_{-\infty}^{\infty} \frac{e^{-t^2}}{(x - t)^2 + y^2} dt + \frac{i}{\pi} \int_{-\infty}^{\infty} \frac{(x - t)e^{-t^2}}{(x - t)^2 + y^2} dt, \\
& \quad (A.4)
\end{aligned}
$$

where is the real part, $\text{Re}[W(x, y)] = \sqrt{2\pi}\sigma V(\lambda, \sigma, \gamma)$ if $x = \frac{\lambda}{\sqrt{2}\sigma}$ and $y = \frac{\gamma}{\sqrt{2}\sigma}$, which can be obtained by using the complex argument, $z = \frac{\lambda + i\gamma}{\sqrt{2}\sigma}$, in the complex probability function. If $\text{Im}[z] \geq 0$, which is always guaranteed for the width of a spectral profile, the complex probability function equals the complex error function. The complex error function has numerous, fast, numerical approximations where in this work we use the `scipy.special.wofz` (Jones et al. 2001) implementation.

Appendix B: Notes on Individual objects

Appendix B.1: GRB090313 (z = 3.373)

Appendix B.2: GRB090530 (z = 1.266)

Appendix B.3: GRB090809 (z = 2.737)

Appendix B.4: GRB090926 (z = 2.106)

Appendix B.5: GRB091018 (z = 0.971)

Appendix B.6: GRB091127 (z = 0.49)

Appendix B.7: GRB100205A (z = na)

Observed 3 days after the *Swift* trigger. No afterglow or host detected in 10.8 ks. GRB likely located at high redshift[7]. The spectrum has not otherwise been published previously.

Appendix B.8: GRB100219A (z = 4.667)

The data presented here also formed the basis of GCN # 10441[8] and is published in Thöne et al. (2013). Observations started 12.5 hours after the *Swift* trigger and has a total exposure time of 4.8 ks. Absorption features, including those of Lyα, from a multitude of ions are detected against the afterglow continuum at $z = 4.667$. Additionally, absorption from an intervening system is found at $z = 2.181$.

Appendix B.9: GRB100316B (z = 1.180)

The data presented here also formed the basis of GCN # 10495[9]. The spectrum has not otherwise been published previously. Observations started 44 minutes after the *Swift* trigger and has a total exposure time of 2.4 ks. Absorption features from Fe II, Al II, Al III, Mg II and Mg I are well detected against the afterglow continuum at $z = 1.180$. Additionally, strong absorption lines from Fe II and Mg II from an intervening system are found at $z = 1.063$.

Appendix B.10: GRB100316D (z = 0.059)

The data presented here also formed the basis of GCN # 10512[10], GCN # 10513[11], GCN # 10543[12] and is published in Bufano et al. (2012) and Starling et al. (2011). This GRB is very close by and has an associated SN, SN2010bh, and has therefore undergone intense follow-up. The data presented here consists of a subset of the entire VLT/X-shooter campaign, covering the four first observing days while the afterglow still contributes significantly to the total emission. The first observations started 10 hours after the burst, before the SN was discovered, and targeted the star-forming 'A'-region(Starling et al. 2011), not the GRB. A very rich spectrum containing a multitude of emission lines puts the host at $z = 0.059$. For three consecutive nights, 58, 79 and 101 hours after the *Swift* trigger, the afterglow was observed as it transitioned into the spectrum of a high-velocity Ic-BL SN. The observations taken 79 and 101 hours after the burst are taken under programme 084.D-0265(A) (PI: Benetti), but with an identical setup to the first two observations.

---

[7] http://gcn.gsfc.nasa.gov/gcn3/10399.gcn3
[8] http://gcn.gsfc.nasa.gov/gcn3/10441.gcn3
[9] http://gcn.gsfc.nasa.gov/gcn3/10495.gcn3
[10] http://gcn.gsfc.nasa.gov/gcn3/10512.gcn3
[11] http://gcn.gsfc.nasa.gov/gcn3/10513.gcn3
[12] http://gcn.gsfc.nasa.gov/gcn3/10543.gcn3

Appendix B.11: GRB100418A (z=0.624)

The data presented here also formed the basis of GCN # 10620[13] and GCN # 10631[14] and is published in De Ugarte Postigo et al. (2011). The burst have been followed up in three epochs of observations, 0.4, 1.4, and 2.4 days after the burst, each lasting 4.8 ks. The unambiguous redshift of the host, $z = 0.624$, is found from the simultaneous detection of emission features belonging to nebular lines, including H I, [O II], [O III], [Ne III], [N II], [S II], [S III], and [He I] as well as absorption features due to the presence of Zn II, Cr II, Fe II, Mn II, Mg II, Mg I, Ti II, and Ca II, all at a consistent redshift. Temporal evolution of the fine structure lines belonging to Fe II* is found between the epochs.

Appendix B.12: GRB100424A (z=2.465)

The data presented here also formed the basis of GCN # 14291[15]. The spectrum has not otherwise been published previously. Observations carried out, long after the burst has faded. Emission lines from the host are detected at $z = 2.465$.

Appendix B.13: GRB100425A (z=1.1755)

The data presented here also formed the basis of GCN # 10684[16] and is used in Skuladottir (2010), but not published elsewhere. Observations started 4 hours after the *Swift* trigger, totaling 2.4 ks. Absorption features from Mg II and Fe II in the afterglow continuum are detected at $z = 1.1755$.

Appendix B.14: GRB100615A (z=1.398)

The data presented here also formed the basis of GCN # 14264[17], but not published elsewhere. Host observation of a dark burst(D'Elia & Stratta 2011) taken long after the afterglow has faded. Emission lines from the host belonging to [O II], [Ne III], [O III] and Hα are detected at a common redshift of $z = 1.398$.

Appendix B.15: GRB100621A (z=0.542)

The data presented here also formed the basis of GCN # 10876[18], but not published elsewhere. Beginning 7.1 hours after the GRB, 2.4 ks observations reveal emission lines from [O II], Hβ and [O III] at a common redshift of $z = 0.542$ and a very weak afterglow continuum.

Appendix B.16: GRB100625A (z=0.452)

The data presented here is of the candidate host galaxy, taken long after the burst has faded and have not previously been published. 4.8 ks of exposure reveals a weak continuum present in all arms, but an absence of emission lines. This could indicate that the host primarily contains a older stellar population. The redshift, $z = 0.452$, is taken from Fong et al. (2013).

Appendix B.17: GRB100724A* (z = 1.288)

The data presented here also formed the basis of GCN # 10971[19]. The spectrum has not otherwise been published previously. The observations were carried out in RRM starting 11 min after the GRB trigger. See section 2.2.1, for a description of the RRM scheme. Absorption lines from several ionic species are detected in the afterglow continuum at a common redshift of $z = 1.288$. This is not a part of the statistical sample.

Appendix B.18: GRB100728B (z=2.106)

The data presented here also formed the basis of GCN # 11317[20]. The spectrum has not otherwise been published previously. Starting 22 hours after the burst trigger, 7.2 ks of observations reveals a faint afterglow continuum with Lyα- and Mg II-absorption at $z = 2.106$. Due to a malfunctioning ADC, the sensitivity of X-shooter is depressed with respect to normal operations, resulting in a poorer throughout. Additionally, the position of the trace on the slit moves due to atmospheric differential refraction.

Appendix B.19: GRB100814A (z=1.439)

The spectra presented here has not been published previously. The observations consists of three visits, the first beginning only 0.9 hours after the *Swift* trigger, the other two visits were 2.13 and 98.40 hours after the trigger, respectively. A bright afterglow continuum is present in all visits, allowing identification of absorption features belonging to a wide range of ions at $z = 1.439$. A complex velocity structure in the absorption features belonging to Mg II, shows several components, separated by as much as 500km/s, pointing to a likely merger scenario in the host.

Appendix B.20: GRB100816A (z=0.805)

The data presented here also formed the basis of GCN # 11123[21]. The spectrum has not otherwise been published previously. This short GRB was observed 28.4 hours after the GRB trigger. 4 x 1200 s of exposure reveals two distinct sets of emission lines, spatially offset $\lesssim 1''$, very close in redshift space, $z = 0.8034$ and $z = 0.8049$, indicating either an interacting host or some complex velocity structure of the host. Faint underlying continua are present under both sets of lines.

Appendix B.21: GRB100901A (z=1.408)

The data presented here has been published in Hartoog et al. (2013). Because of the unusual lingering brightness of this GRB, 2.4s of observations taken 65.98 hours after the GRB trigger still reveals an afterglow continuum visible across the entire spectral coverage of X-shooter. Absorption lines from a wide range ion put the redshift at $z = 1.408$, with intervening absorption systems at $z = 1.3147$ and $z = 1.3179$.

Appendix B.22: GRB101219A (z=0.718)

This data has not been published before. Starting 3.7 hours after the GRB trigger, 7.2 ks of exposure time reveals a very faint continuum in the visual and near-infrared, only visible when heavily

---

[13] http://gcn.gsfc.nasa.gov/gcn3/10620.gcn3
[14] http://gcn.gsfc.nasa.gov/gcn3/10631.gcn3
[15] http://gcn.gsfc.nasa.gov/gcn3/14291.gcn3
[16] http://gcn.gsfc.nasa.gov/gcn3/10684.gcn3
[17] http://gcn.gsfc.nasa.gov/gcn3/14264.gcn3
[18] http://gcn.gsfc.nasa.gov/gcn3/10876.gcn3

[19] http://gcn.gsfc.nasa.gov/gcn3/10971.gcn3
[20] http://gcn.gsfc.nasa.gov/gcn3/11317.gcn3
[21] http://gcn.gsfc.nasa.gov/gcn3/11123.gcn3

binning the images. No redshift estimate is available from these observations. Late-time Gemini-North observations reveal emission lines from the host at $z = 0.718$[22].

Appendix B.23: GRB101219B (z=0.552)

The data presented here also formed the basis of GCN # 11579[23] and is published in Sparre et al. (2011). The first observation, taken 11.6 hours after the burst trigger and lasting 4.8ks, reveals absorption from Mg II and Mg I in the host located at $z = 0.552$ on a featureless continuum visible across the entire coverage of X-shooter. Subsequent observations taken 16 and 37 days after the trigger shows the fading spectral signature of a SN, SN2010ma.

Appendix B.24: GRB110128A (z=2.339)

Appendix B.25: GRB110407A (z=na)

Appendix B.26: GRB110709B (z=na)

Appendix B.27: GRB110715A (z=0.82)

Appendix B.28: GRB110721A (z=0.382)

Appendix B.29: GRB110808A (z=1.348)

Appendix B.30: GRB110818A (z=3.36)

Appendix B.31: GRB111005A (z=0.013)

Appendix B.32: GRB111008A (z=4.989)

Appendix B.33: GRB111107A (z=2.893)

Appendix B.34: GRB111117A (z=1.3?)

Appendix B.35: GRB111123A (z=3.151)

Appendix B.36: GRB111129A (z=na)

Appendix B.37: GRB111209A (z=0.677)

Appendix B.38: GRB111211A (z=0.478)

Appendix B.39: GRB111228A (z=0.716)

Appendix B.40: GRB120118B (z = 2.943)

The data presented here also formed the basis of GCN # 14225[24], but is not published otherwise. This late-time observation of the host of GRB120118B consists of 3.6 ks exposures and contains emission lines belonging to [O II]and [O III]at $z = 2.943$, suggested to be redshift of the host.

Appendix B.41: GRB120119A (z = 1.728)

The data presented here has not been published before. Three epochs of observations have been obtained, the first two immediately after the burst, and the last one long after the afterglow had faded. Starting 1.4 hours after the *Swift* trigger, the first epoch contains bright afterglow continuum. Rich in absorption features belonging to a multitude of ions, $z = 1.728$ is estimated for the host with intervening systems at $z = 1.476$, $z = 1.214$, $z = 0.662$ and $z = 0.632$. The second epoch, obtained 4.5 hours after the burst contains the fading afterglow. A third epoch is obtained > 1

year after the GRB in which emission lines from Hβ and Hα are found at the redshift of the host, confirming the association of the absorption line system and the host.

Appendix B.42: GRB120211A (z = 2.346)

The data presented here has been published in Krühler et al. (2015). Two observations of the host of GRB120211A has been obtained, starting 2013.02.17, $> 1 year$ after the burst has faded. A redshift for this object has been reported by Krühler et al. (2015) and the features seen by those authors are reproduced in these reductions, confirming $z = 2.346$.

Appendix B.43: GRB120224A (z = 1.10 NEW!!!)

The data presented here has formed the basis of GCN # 12991[25], and has also been published in Krühler et al. (2015). Starting 19.8 hours after the GRB trigger, a total exposure time of 2.4 ks reveals a faint continuum, starting at ~ 7000 Å and extending all the way through 25000 Å. We detect a $\sim 2\sigma$ emission line which, if interpreted as Hα, gives $z = 1.10$, supporting the redshift reported by Krühler et al. (2015).

Appendix B.44: GRB120311 (z = 0.350 NEW!!!)

The data presented here has formed the basis of GCN # 12991[26], but is not published otherwise. Starting just before twilight, 3.65 hours after the burst, a faint afterglow continuum is detected at all wavelengths. Due to the faintness of the afterglow, no absorption features are discernible superposed on the continuum. Displaced from the afterglow continuum by 1$''$4, emission lines belonging to Hβ, [O III] and Hα are detected at $z = 0.350$. The line belonging to Hα shows some extended emission toward the afterglow continuum. The angular distance between the two sources correspond to a projected distance in the host plane of 6 kpc, posing a potential problem for the host redshift, unless the GRB ocurred in a merging system. The extended emission in Hα, supports this interpretation. This burst is not apart of the statistical sample.

Appendix B.45: GRB120327A (z = 2.813)

The data presented here also formed the basis of GCN # 13134[27] and is published in D'Elia et al. (2014). The observation consists of two visits, 2.13 hrs and 29.98 hrs after the burst, with an afteglow continuum visible in all arms for both visits. We detect absorption features from Ly-limit, Lyα, C II/C II*, Si II/Si II*, Al I, Fe II and Mg II are detected at a consistent redshift, $z = 2.813$.

Appendix B.46: GRB120404A (z = 2.876)

The data presented here has formed the basis of GCN # 13227[28], but is not published otherwise. 9.6 ks integration, starting 15.7 hours after the *Swift*-trigger reveals a low-intensity afterglow continuum on which absorption from Ly$\alpha$is detected in two distinct regions at redshifts $z = 2.876$ and $z = .255$. These absorption systems are confirmed by ionic absorption features at both of these redshifts.

[22] http://gcn.gsfc.nasa.gov/gcn3/11518.gcn3
[23] http://gcn.gsfc.nasa.gov/gcn3/11579.gcn3
[24] http://gcn.gsfc.nasa.gov/gcn3/14225.gcn3
[25] http://gcn.gsfc.nasa.gov/gcn3/12991.gcn3
[26] http://gcn.gsfc.nasa.gov/gcn3/12991.gcn3
[27] http://gcn.gsfc.nasa.gov/gcn3/13134.gcn3
[28] http://gcn.gsfc.nasa.gov/gcn3/13227.gcn3

Appendix B.47: GRB120422A (z = 0.283)

The data presented here also formed the basis of GCN # 13257[29] and is published in Schulze et al. (2014). A GRB-SN, this burst has been followed up multiple times. The data presented here only contain the first epoch in which the afterglow is still visible and before the rise of SN2012bz. Starting 16.5 hours after the burst, 4.8 ks integration time captures both the host and the burst in emission. A blue afterglow continuum is detected at all wavelengths covered by X-shooter, on which Mg ɪɪabsorption at $z = 0.283$ is found. Offset by 1″.75, the host is clearly detected at a consistent redshift with a rich emission line spectrum, the lines extending towards to burst.

Appendix B.48: GRB120712A (z = 4.175)

The data presented here also formed the basis of GCN # 13460[30] and is not published elsewhere. 4.8 ks integration time, starting 10.5 hours after the BAT trigger, shows a bright afterglow continuum starting at ~ 4720 Å, signifying the onset of the Lyman alpha forest, for a GRB located at $z = 4.175$. Absorption features from Lyα, Fe ɪɪ, Mg ɪɪ and Si ɪɪ are readily detected at a consistent redshift.

Appendix B.49: GRB120714B (z = 0.398)

The data presented here also formed the basis of GCN # 13477[31], but is not published elsewhere. Observations of this burst started 7.8 hours after the GRB trigger, lasting 4.8 ks. A continuum is visible across the entire spectral coverage of X-shooter, with both emission lines from [O ɪɪ], Hβ, [O ɪɪɪ] and Hα, as well as absorption from Mg ɪɪ detected at $z = 0.398$, securely setting it as the redshift of the GRB.

Appendix B.50: GRB120716A (z = 2.486)

The data presented here also formed the basis of GCN # 13494[32], but is not published elsewhere. Despite observations starting 62 hours after the *Swift* trigger and lasting 3.6 ks, a bright afterglow is clearly seen, along with a plethora of absorption features. Absorption of Lyα-photons in the host leaves a broad trough, from which the Lyman alpha forest is visible bluewards, all the way down to the Lyman limit. Metal absorption lines from C ɪɪ, Si ɪɪ, [O ɪ], Fe ɪɪ, C ɪᴠ, Si ɪᴠ, including fine structure transitions identified as C ɪɪ*, Si ɪɪ*, Fe ɪɪ* and metastable [Ni ɪɪ] lines are all detected at $z = 2.486$

Appendix B.51: GRB120722A (z = 0.959)

The data presented here also formed the basis of GCN # 13507[33], but is not published elsewhere. On 4.8 ks integration time, starting 10 hours after the burst trigger, the simultaneous detection of absorption features belonging to Mg ɪɪ and Fe ɪɪ superposed on a blue continuum, and emission lines from [O ɪɪ], Hγ, Hβ, [O ɪɪɪ] and Hα, all at $z = 0.959$, confidently sets it as the redshift of the GRB.

Appendix B.52: GRB120805A (z ∼ 3.9 NEW!!!)

A separate reduction of this burst has been published in Krühler et al. (2015), but not otherwise. Starting 9 days after the burst trigger, this is host observation and does not contain any afterglow continuum. In 3.6 ks integration time, we detect a faint continuum visible from 4500 Å and all the way through 21000 Å, in contrast to what is found previously. The continuum from 4500 - 6000 Åis detected at very low significance. If the drop at 4500 Å is the Lyman limit, this fits with Lyman alpha at ∼ 6000 Å, giving $z \sim 3.9$. The absence of nebular lines if due to [O ɪɪ] falling in a telluric absorption band and the rest being shifted out of the wavelength coverage.

Appendix B.53: GRB120815A* (z = 2.358)

Not a part of the statistical sample, thisburst also formed the basis of GCN # 13649[34] and is published in Krühler et al. (2013). Observations started 1.69 hours after the BAT trigger and consist of 2.4 ks integration. A bright afterglow continuum is detected across the entire spectral coverage of X-shooter, with a multitude of absorption lines superposed. Absorption features from the host at $z = 2.358$ include a DLA as well as metal absorption lines from [N ᴠ], [S ɪɪ], Si ɪɪ, [O ɪ], C ɪᴠ, Si ɪᴠ, Fe ɪɪ, Al ɪɪ, Al ɪɪɪ, Mn ɪɪ, Mg ɪɪ, and Mg ɪ. Additionally fine structure lines from [Ni ɪɪ]and Fe ɪɪare exited local to the GRB. Intervening systems are found at $z = 1.539$, $z = 1.693$, and $z = 2.00$.

Appendix B.54: GRB120909A (z = 3.929)

The data presented here has formed the basis of GCN # 13730[35], but is not published otherwise. A very rapid follow-up, starting only 1.7 hours after the BAT trigger, this 1.2 ks observation captures a very bright afterglow continuum, starting at 4500 Å, signifying the onset of the Lyman limit for a system at $z = 3.929$. Absorption from high-column density hydrogen leaves very prominent absorption features in the form of Lyα, Lyβ, and Lyγ, visible in the Lyman alpha forest. Metal absorption lines arising from Fe ɪɪ, [Ni ɪɪ], Si ɪɪ, [S ɪɪ], Al ɪɪ, Al ɪɪɪ, C ɪɪ, [O ɪ], C ɪᴠ, and Zn ɪɪ are all detected along with the corresponding fine structure lines from (Fe ɪɪ*, Si ɪɪ*, [O ɪ]*, [O ɪ]**, C ɪɪ*), securely anchoring the redshift of the host.

Appendix B.55: GRB120923A (z = ≳ 8 ?)

Appendix B.56: GRB121024A (z = 2.300)

The data presented here also formed the basis of GCN # 13890[36] and is published in Friis et al. (2015). Also rapid, starting 1.8 hours after the *Swift* trigger, a bright afterglow continuum is visible across all arms. A broad absorption feature from Lyman alpha, along with narrow lines from C ɪᴠ, Si ɪɪ, Si ɪᴠ, Fe ɪɪ, [S ɪɪ], and Al ɪɪ, as well as fine structure lines associated with Si ɪɪ* are all detected at $z = 2.300$, securely setting it as the redshift of the GRB.

---

[29] http://gcn.gsfc.nasa.gov/gcn3/13257.gcn3
[30] http://gcn.gsfc.nasa.gov/gcn3/13460.gcn3
[31] http://gcn.gsfc.nasa.gov/gcn3/13477.gcn3
[32] http://gcn.gsfc.nasa.gov/gcn3/13494.gcn3
[33] http://gcn.gsfc.nasa.gov/gcn3/13507.gcn3

[34] http://gcn.gsfc.nasa.gov/gcn3/13649.gcn3
[35] http://gcn.gsfc.nasa.gov/gcn3/13730.gcn3
[36] http://gcn.gsfc.nasa.gov/gcn3/13890.gcn3

Appendix B.57: GRB121027A (z = 1.773)

The data presented here has formed the basis of GCN # 13930[37], but is not published otherwise. Starting 69.6 hours after the GRB trigger, that we detect the afterglow continuum a so high significance in all arms with 8.4 ks integration, testifies to the brightness of this burst. The concurrent identification of emission lines from [O ɪɪɪ] and absorption from C ɪv, Al ɪɪ, Al ɪɪɪ, Mg ɪ, Mg ɪɪ, and Fe ɪɪ, tightly constrains the redshift of the burst to be ($z = 1.773$

Appendix B.58: GRB121201A (z = 3.385)

Appendix B.59: GRB121229A (z = 2.707)

Appendix B.60: GRB130131B (z = 2.539)

Appendix B.61: GRB130408A (z = 3.758)

The data presented here also formed the basis of GCN # 14365[38]. The spectrum has not otherwise been published previously. The observations consists of two 600sec spectra taken 1.9hrs after the burst. We detect absorption features from a wide range of ions. We also detect intervening absorption at $z = 1.255$ and $z = 3.248$.

Appendix B.62: GRB130418A (z = 1.218)

Appendix B.63: GRB130427A (z = 0.34)

Appendix B.64: GRB130427B (z = 2.78)

Appendix B.65: GRB130603B (z = 0.356)

Appendix B.66: GRB130606A (z = 5.913)

The data presented here also formed the basis of GCN # 14816[39] and is published in Hartoog et al. (2015). The observations consists of three 2x600sec visits starting 7.1 hrs after the burst at fairly high airmass. We detect absorption features from a wide range of ions at $z = 5.913$ as well as intervening absorption at $z = 2.3103, 2.5207, 3.4515, 4.4660, 4.5309, 4.5427, 4.6497$ and 4.7244.

Appendix B.67: GRB130612A (z = 2.006)

Appendix B.68: GRB130615A (z = 3?)

Appendix B.69: GRB130701A (z = 1.155)

Appendix B.70: GRB131011A (z = 1.874)

Appendix B.71: GRB131030A (z = 1.296)

Appendix B.72: GRB131103A (z = 0.599)

Appendix B.73: GRB131105A (z = 1.686)

Appendix B.74: GRB131117A (z = 4.042)

Appendix B.75: GRB131231A (z =0.642)

Appendix B.76: GRB140114A (z = ~ 2.8?)

Appendix B.77: GRB140213A (z = 1.208)

Appendix B.78: GRB140301A (z = 1.416)

Appendix B.79: GRB140311A (z = 4.95)

Appendix B.80: GRB140430A (z = 1.601)

Appendix B.81: GRB140506A (z = 0.889)

Appendix B.82: GRB140515A (z = ~ 6.32?)

Appendix B.83: GRB140614A (z = 4.233)

Appendix B.84: GRB140622A (z = 0.959)

Appendix B.85: GRB141028A (z = 2.332)

Appendix B.86: GRB141031A (z = na)

Appendix B.87: GRB141109A (z = 2.993)

Appendix B.88: GRB150206A (z = 2.087)

Appendix B.89: GRB150301B (z = 1.517)

Appendix B.90: GRB150403A (z = 2.06)

Appendix B.91: GRB150423A (z = 1.394)

Appendix B.92: GRB150428A (z = na)

Appendix B.93: GRB150514A (z = 0.807)

Appendix B.94: GRB150518A (z = 0.256)

Appendix B.95: GRB150616A (z = 1.188)

Appendix B.96: GRB150727A (z = 0.313)

Appendix B.97: GRB150821A (z = 0.755)

Appendix B.98: GRB150831A (z = na)

Appendix B.99: GRB150910A (z = 1.359)

Appendix B.100: GRB150915A (z = 1.968)

Appendix B.101: GRB151021A (z = 2.330)

The data presented here also formed the basis of GCN # 18426[40] and is not published elsewhere. The observation was carried out in RRM starting 44 minutes after the GRB trigger. We detect absorption features from a wide range of ions at $z = 2.330$ as well as intervening absorption at $z = 1.49$.

---

[37] http://gcn.gsfc.nasa.gov/gcn3/13930.gcn3
[38] http://gcn.gsfc.nasa.gov/gcn3/14365.gcn3
[39] http://gcn.gsfc.nasa.gov/gcn3/14816.gcn3
[40] http://gcn.gsfc.nasa.gov/gcn3/18982.gcn3

Appendix B.102: GRB151027B (z = 4.063)

Appendix B.103: GRB151029A (z = 1.423)

Appendix B.104: GRB151031A (z = 1.167)

Appendix B.105: GRB160117B (z = 0.87)

Appendix B.106: GRB160203A (z = 3.517)

The data presented here also formed the basis of GCN # 18982[41] and is not published elsewhere. The observation was carried out in RRM starting 18 minutes after the GRB trigger. We detect absorption features from a wide range of ions at $z = 3.517$ as well as intervening absorption at $z = 2.203$.

Appendix B.107: GRB160228A (z = 1.64)

Appendix B.108: GRB160303A (z = na)

Appendix B.109: GRB160314A (z = 0.726)

Appendix B.110: GRB160410A (z = 1.717)

Appendix B.111: GRB160425A (z = 0.555)

Appendix B.112: GRB160625B (z = 1.406)

Appendix B.113: GRB160804A (z = 0.736)

The data presented here also formed the basis of GCN # 19773[42], but is not published elsewhere. Observations started 22.37 hours after the BAT trigger and lasted for 2.4ks. The afterglow continuum is detected across the entire spectral coverage of X-shooter and absorption lines from Mg I, Mg II, Fe II and Al II are found at $z = 0.736$. At the same redshift, emission lines from [O II], [O III], Hα, Hβ, Hγ, [N II], [S II], [S III] are found. A second epoch, lasting 3.6ks, is obtained after the afterglow has faded, confirming the emission line detections.

Appendix B.114: GRB161001A (z = 0.891?)

Appendix B.115: GRB161007A (z =4.6 ??? NEW!!!)

This data has not been published elsewhere. Observations for GRB161007A started 323 hours after the burst trigger and contains the potential host. 4 x 600 seconds of observations reveals a faint continuum rising abruptly above the noise at $\sim$ 6850 Å and continuing through 21000 Å. A very low significance continuum is detected at shorter wavelengths, down to $\sim$ 6000 Å. If the host is located at $z \sim 4.6$, the drop in continuum flux is the Lyman alpha break and the absence of nebular emission lines is due to [O II]being shifted out of the wavelength coverage. Alternatively, an early-type host at $z = 0.71$ could exhibit the 4000 Åbreak at 6000 Å, but due to the preference of long-duration GRBs for star-forming galaxies, this is the least likely explanation, why we believe the high-z solution.

Appendix B.116: GRB161014A (z =2.823)

The data presented here also formed the basis of GCN # 20061[43], but is not published elsewhere. Starting 11.6 hours after the GRB trigger, 4.8 ks of integration time captures the afterglow continuum across all three spectroscopic arms. A broad absorption trough due to Lyman alpha is visible, along with metal absorption features from Mg II, Si II, C II, C IV, Al II, Al III, and Fe II, all at $z = 2.823$. Similar to GRB140506 (Fynbo et al. 2014), a break in the continuum shape is detected bluewards of 6000Å, possible signifying some anomalous form of extinction.

Appendix B.117: GRB161023A (z = 2.710)

Appendix B.118: GRB161117A (z = 1.549)

---

[41] http://gcn.gsfc.nasa.gov/gcn3/18982.gcn3
[42] http://gcn.gsfc.nasa.gov/gcn3/19773.gcn3
[43] http://gcn.gsfc.nasa.gov/gcn3/20061.gcn3